FABRICATION AND CHARACTERIZATION OF CARBON NANOTUBES FOR BIOMEDICAL APPLICATIONS

by

Zhiyang Rong

A Thesis

Submitted to the Faculty

of the

WORCESTER POLYTECHNIC INSTITUTE

in partial fulfillment of the requirements for the

Degree of Master of Science

in

Mechanical Engineering

August 2008

APPROVED:

Dr. Jianyu Liang, Advisor	Dr. Hong Zhou, Committee member
Dr. Cosme Furlong, Graduate committee representative	Dr. Richard D. Sisson, Jr., Committee member

ABSTRACT

Recently, nanomaterials have been vigorously studied for the development of biosensors. Among them, carbon nanotubes (CNTs) have stimulated enormous interest for constructing biosensors due to their unique physical and chemical properties such as high surface-to-volume ratio, high conductivity, high strength and chemical inertness. Our study is to develop a general design of biosensors based on vertically aligned CNT arrays. Glucose biosensor is selected as the model system to verify the design of biosensors. In the preliminary design, glucose oxidase (GOx) is attached to the walls of the porous alumina membrane by adsorption. Porous highly ordered anodized aluminum oxide (AAO) prepared by two-step anodization are used as templates. Deposited gold on both sides of template surfaces serve as a contact and prevent non-specific adhesion of GOx on the surface. In order to find out optimized thickness of gold coating, the oxidation and reduction (redox) reaction in $[Fe(CN)_6]^{3-}$ /$[Fe(CN)_6]^{4-}$ system is monitored by Cyclic Voltammetry (CV). Subsequently, enzymatic redox reaction in glucose solutions is also attempted by CV. We expect protein layers with GOx form a conductive network. However, no obvious enzymatic redox reaction is detected in the voltammogram. To take advantage of the attractive properties of CNTs, the design of enzyme electrodes is modified by attaching CNT onto the sidewalls of AAO template nanopores and then immobilizing GOx to the sidewalls and tips of CNTs. AAO templates provided vertical, parallel, well separated and evenly spacing nanochannels for CNT growth. Cobalt is used as a catalyst to fabricate CNTs. As a result, multi-walled carbon nanotubes (MWCNTs) are fabricated

inside the AAO templates by catalytic chemical vapor deposition (CCVD). Characterization of AAO templates and cobalt electrochemical deposition are employed by scanning electron microscope (SEM), and energy dispersive X-ray spectrometry (EDS). Detailed structure and texture of CNTs are examined by transmission electron microscope (TEM).

ACKNOWLEDGMENTS

I would like to sincerely thank my advisor Dr. Jianyu Liang for being such an incredible mentor during my graduate period. Professor Liang is a diligent person with great energy. Her passion for work has deeply impressed me. I have also been motivated by her keen perspective on academic research. Throughout the whole project, she gave me many precious suggestions and has always been ready to answer my questions. I'm very glad that I had a chance to work in her Nanomaterials and Nanomanufacturing Laboratory for the past two years. It leaves me with a most valuable memory in my academic life. I have learned more than I could ever image.

I would also like to thank all my colleagues at WPI. In particular, I'd like to thank Dr. Boquan Li, who has provided me with training on the SEM and TEM. Dr. Li is an accommodating person. Without his help, I would not be able to take any SEM or TEM images for my thesis. Additionally, I'd like to thank all the members in our group: Shelley Dougherty, Huanan Duan, Dawei Zhang and Ryan Blair. They are all warmhearted people who have helped me in my research and thesis. As the eldest graduate students in our lab, Shelley and Huanan have taught me a lot during the experiments. Shelley has collaborated on some of my earliest work. Without her initially getting me started, I would have taken a much longer time to get on the right track. Huanan has always been willing to share his broad knowledge with me. Thanks to his demonstration on the fabrication of anodized aluminum oxidase, I was able to continue my research much further. I would also like to thank, Dawei Zhang and Ryan, who have made their efforts in improving my thesis.

Additionally, I would like to give my special thank to my family: my father (Yixiang Rong), my mother (Pei Qi), my uncle (Yiming Rong) and my aunt (Jiaoshi Dong). They encouraged me to attend graduate college abroad and have been inspirational throughout my life. Without their great love and lifelong support, I certainly would not be able to achieve what I've done.

Finally, I would like to thank my friends Yue Wang, Dong Lu, Xuekun Li, Hua Li, Lei Zhang and Feng Liu. All of you have made my days at WPI very unforgettable.

TABLE OF CONTENTS

LIST OF FIGURES

LIST OF TABLES

ABBREVIATIONS AND SYMBOLS

AAO	anodized aluminum oxide
AFM	atomic force microscopy
APA	3-amino propylphosphonic acid
CCVD	catalytic chemical vapor deposition
CNTs	carbon nanotubes
CV	cyclic voltammetry
DET	direct electron transfer
EDS	energy dispersive spectrometer
FAD	flavin adenine dinucleotide
$[Fe(CN)_6]^{3-}$	ferricyanide
$[Fe(CN)_6]^{4-}$	ferrocyanide
GA	glutaraldehyde
GOx	glucose oxidase
MWCNTs	multi-walled carbon nanotubes
redox	oxidation and reduction
sccm	standard-state cubic centimeter per minute
SCE	saturated calomel electrode
SEM	scanning electron microscopy
SHE	standard hydrogen electrode
STM	scanning tunneling microscopy
SWCNTs	single-walled carbon nanotubes

TEM	transmission electron microscopy
XRD	X-ray diffraction
θ	chiral angle
ΔE	peak separation
A	electrode area
C	concentration
$\vec{C}$	chiral vector
D	diffusion coefficient
E^0	standard redox potential
$E_{1/2}$	polarographic half-wave potential
E_p	peak potential
$E_{p/2}$	half-peak potential
n	number of electrons
T	tube axis
v	potential scan rate

1. Introduction

1.1 Introduction to carbon nanotubes (CNTs)

Carbon nanotubes (CNTs) are rolled up cylinders of graphene sheets. They were first observed as multi-walled carbon nanotubes (MWCNTs) by Dr. Iijima in 1991 [1]. Figure 1.2 shows the high resolution transmission electron microscope (TEM) images of the MWCNTs. These tubes are composed of 2 to 50 coaxial graphitic carbon sheets with smallest inner diameter of around 2nm and length up to 1 μm. Two years later,

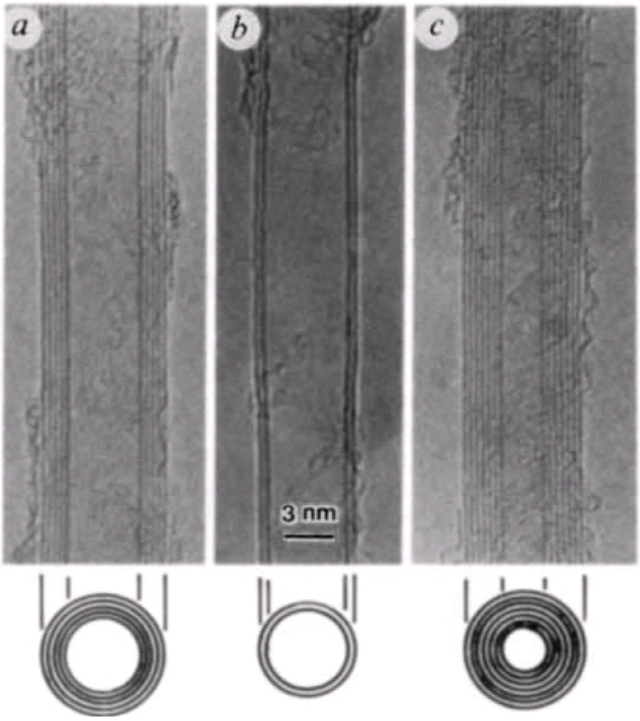

Figure 1.2 High resolution TEM images of MWCNTs, showing different diameters and diverse numbers of graphene sheets [1].

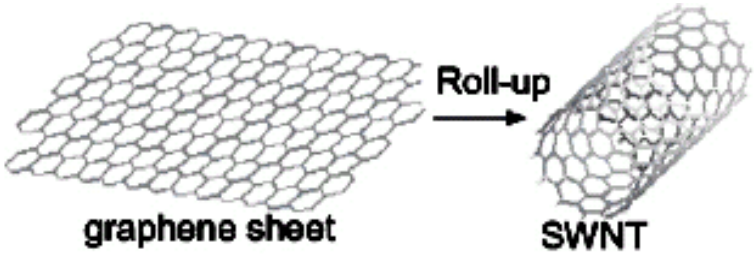

Figure 1.1 Rolling of graphite sheet into a SWCNT [4].

Iijima [2] and Bethune [3] both reported the observation of single-walled carbon nanotubes (SWCNTs), which was a new nanomaterial to the scientists. Figure 1.1 shows how graphene sheet can be rolled up to SWCNTs. Its unique structure leads to attractive physical and chemical properties such as high conductivity and good mechanical strength. Ever since, these properties have stimulated great interest of many researchers and shown tremendous potential in various applications such as electronics [5], mechanics [6], chemistry and biology [7].

1.1.1 Structure of CNTs

There are two distinct families of carbon nanotubes, MWCNTs and SWCNTs. SWCNT is a single, seamless, wrapped graphene sheet which has the form of hexagonal aromatic ring patterns. It can be rolled up in many different ways, and the structure of SWCNT can be classified into three basic types: armchair, zigzag and

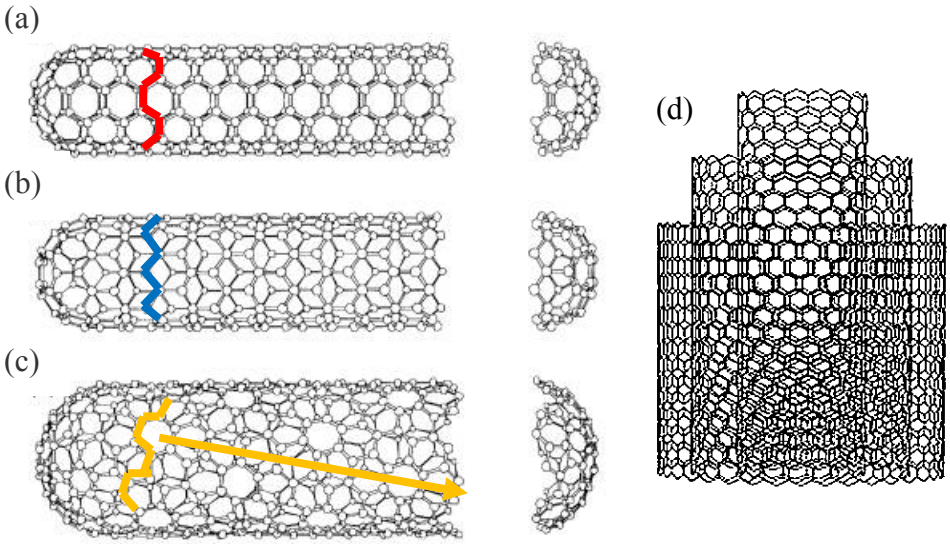

Figure 1.4 Three structures of SWCNTs: (a) armchair, (b) zigzag, (c) chiral nanotubes and (d) the structure of MWCNTs. (Adapted from [8])

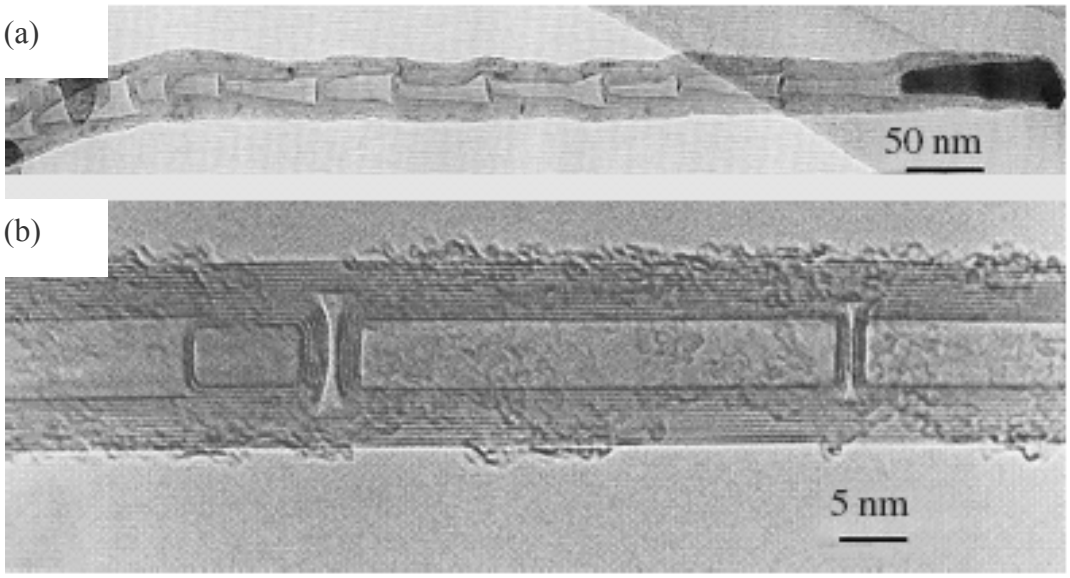

Figure 1.3 Textures of MWCNTs (a) herringbone texture and (b) bamboo texture [8].

chiral (Figure 1.4 (a), (b), (c), respectively). MWCNTs consist of coaxial SWCNT sheets. Figure 1.4 (d) shows the schematic structure of MWCNTs. When MWCNTs were first discovered by Dr. Iijima, the numbers of SWCNT layers varied from 2 to 50 [1]. Theoretically, the coaxial layers are from 2 to infinite [8]. The distance between sheets is 0.34nm [8].

MWCNTs are materials with various textures. Two common features [8] are shown in Figure 1.3. One is the so-called herringbone texture, in which graphene layers are at an angle with respect to the nanotube axis. The other is the so-called "bamboo" texture, in which graphene sheets are oriented perpendicular to the nanotubes axis.

Since MWCNT is constitutive of SWCNT, it is necessary to study the structure of SWCNT first. To simplify the understanding of the structure of SWCNT, we can

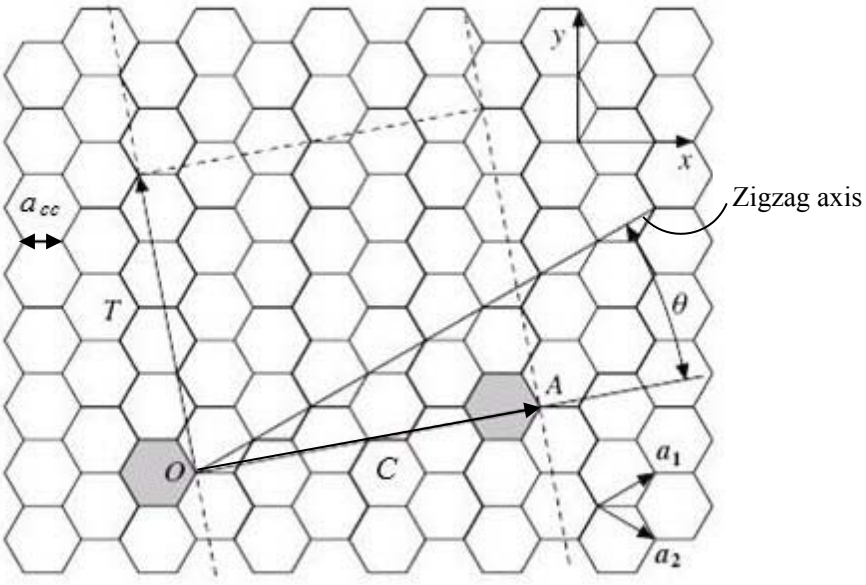

Figure 1.5 Construction of graphene sheet and important parameters for CNTs: $\vec{C}$ is chiral vector, T is tube axis, θ is chiral angle (Adapted from [8]).

consider SWCNT is rolled up by graphene sheet to a nanotube with respect to a certain direction. This direction is known as the tube axis *T* [8], shown in Figure 1.5. Figure 1.5 shows the construction of graphene sheet. Every carbon atom on the sheet can be expressed as a function of integers (n, m). A chiral vector $\vec{C}$ is the vector perpendicular to the tube axis *T*, given by

$$\vec{C} = n\vec{a}_1 + m\vec{a}_2 \tag{1.1}$$

with $\vec{a}_1 = \frac{a\sqrt{3}}{2}\hat{x} + \frac{a}{2}\hat{y}$, $\vec{a}_2 = \frac{a\sqrt{3}}{2}\hat{x} - \frac{a}{2}\hat{y}$, the angle between $\vec{a}_1$ and $\vec{a}_2$ is 60°

where $a = \sqrt{3}a_{cc} = 0.246nm$, a_{cc} is the C=C bond and has a value of 0.142nm.

Based on the direction of chiral vector, the SWCNT is either of the armchair (n=m), zigzag (n=0 or m=0), or chiral (any other n and m). The diameter of the SWCNT is

$$D = \frac{\left|\vec{C}\right|}{\pi} = \frac{a_{cc}\sqrt{3(m^2 + n^2 + nm)}}{\pi} \tag{1.2}$$

The tube axis *T* of the zigzag structure is along a three-fold axis, making its chiral axis the so called the zigzag axis. The chiral angle, representing the chirality of the tube, is the angle between the chiral vector and this zigzag axis. It is expressed as

$$\cos\theta = \frac{2n + m}{2\sqrt{n^2 + m^2 + nm}}, \text{ usually } 0° \le \theta \le 30°. \tag{1.3}$$

Consequently, the chiral angle of the zigzag structure equals to 0° and the armchair structure is 30°.

1.1.2 Properties and applications of CNTs

The unique structures of CNTs result in many attractive properties. In general, the diameters of CNTs are in the nanometer range while the length could be at micro-scale [9]-[11]. SWCNTs have stimulated intense interest for detailed structure and property studies, because the original structure of SWCNTs leads to the novel properties. For instance, SWCNTs are stable up to 750 °C in air and up to 1500-1800 °C in an inert atmosphere [8]. Properties of MWCNTs vary depending on the structure and the texture of MWCNTs. The bond strength is quite different along the in-plane direction and the direction perpendicular to the plane. Along the in-plane direction, very strong covalent strength results in short bonds of 0.142nm [8]. However, in the direction perpendicular to the plane, only very weak Van der Waals forces exist and cause loose bonds of 0.34nm [8]. Such heterogeneity can be observed in bundles of SWNCTs and MWCNTs, but not found in individual SWCNT. Thus, properties of CNTs may change significantly depending on whether MWCNTs or SWCNTs are considered.

SWCNTs are unique nanostructures with unusual electronic properties, because of the one–dimensional quantum effect. Figure 1.6 shows the early prediction that CNTs could be either semi-conducting or metallic depending on their diameter and the chirality of the constituent graphene tubules [12] [13]. For example, the zigzag structure has semi-conductor or quasi-metallic properties whereas the armchair structure behaves as a metallic material. This prediction of CNTs properties was later confirmed experimentally [14] [15]. In the metallic state, the conductivity of the

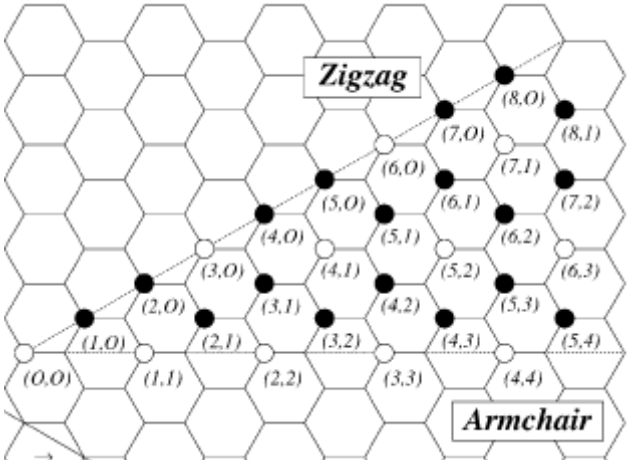

Figure 1.6 Different electronic properties with respect to various chiral angles.● is semi-conductive, while○ is metallic (Adapted from [11]).

carbon nanotubes is very high. It is estimated that they can carry 10^9 A/cm^2 [16]. Copper wire fails at 10^6 A/cm^2 because resistive heating melts the wire. One reason for the high conductivity of the CNTs is that they have very few defects to scatter electrons, and thus a very low resistance. High currents do not heat the tubes in the same way that they heat copper wires. CNTs also have a very high thermal conductivity, allowing them to be very good conductors for heat. The measured room temperature thermal conductivity for an individual SWCNT is more than 6000 W/mK [17] and MWCNT is 3000 W/mK [18], both greater than that of natural diamond and the basal plane of graphite (both 2000 W/mK).

Carbon nanotubes have desirable mechanical properties. They have a combination of high strength and high stiffness. The tensile strength of SWCNTs has been measured equal to about 45 GPa [19] [20], which is 20 times that of steel. Such high tensile strength makes them a promising candidate for reinforcement applications. Early theoretical work and experiments on individual CNTs (mostly MWCNT)

confirmed that they were one of the stiffest structures. The bending modulus of defective MWCNTs was measured to be 2-30 GPa [21]-[23]. They buckle like straws but do not break, and can theoretically be straightened back without any damage. Most materials fracture on bending because of the presence of defects such as dislocations or grain boundaries. However, this does not occur to CNTs, mainly because they have so few defects in the structure of their walls. Another reason why they do not fracture is that as they are bent severely, the almost hexagonal carbon rings in the walls change in structure but do not break, which can be explained by the rehybridization of their sp^2 bonds [16].

CNTs have a high surface-to-volume ratio, high conductivity and are chemically inert. These properties make CNTs an attractive candidate for constructing biosensors. Large surface-to-volume ratio offers large accessible surface. High conductivity offers a good opportunity for direct electron transfer (DET). Their chemical inertness avoids unnecessary noise introduced to the system. On the other hand, CNTs are able to be functionalized to connect to biomolecules. As the reactivity of graphite is known to occur mainly through edges, perfect SWCNTs have almost no chemically active dangling bonds. The chemical reactivity of SWCNTs comes mainly from the caps, where pentagons exist [16]. CNTs with defects or open ends have intrinsically higher reactivity, due to the occurrence of accessible edges at the nanotube surfaces.

The unique properties of CNTs make them promising materials in many inorganic applications such as battery electrodes [24], mechanical reinforcement [25] [26]and nanoprobes [27]. Meanwhile, CNTs show great potential

in biomedical applications such as drug delivery [28] and biosensors [29] [30].

1.1.3 Synthesis of nanotubes growth

1.1.3.1 Electric arc-discharge method

Electric Arc-discharge method has been employed to fabricate CNTs since they were first discovered [1]. An example of an electric arc reactor is shown in Figure 1.7 [8]. A potential (~18V) is applied across two electrodes, which are usually carbon rods of few millimeters in diameter, separated by a certain distance (~1mm) in helium. A high current discharge (~100A) passes through the opposing carbon anode and cathode, where plasma is generated, and carbon atoms are evaporated onto the electrodes. Without catalysts, CNTs are formed as MWCNTs [11]. To produce SWCNTs, a small amount of transition metal (usually iron, cobalt or nickel) is incorporated as a catalyst in the central region of the anode. Bethune and coworkers [3] first produced a substantial amount of SWCNT by arc-discharge method using

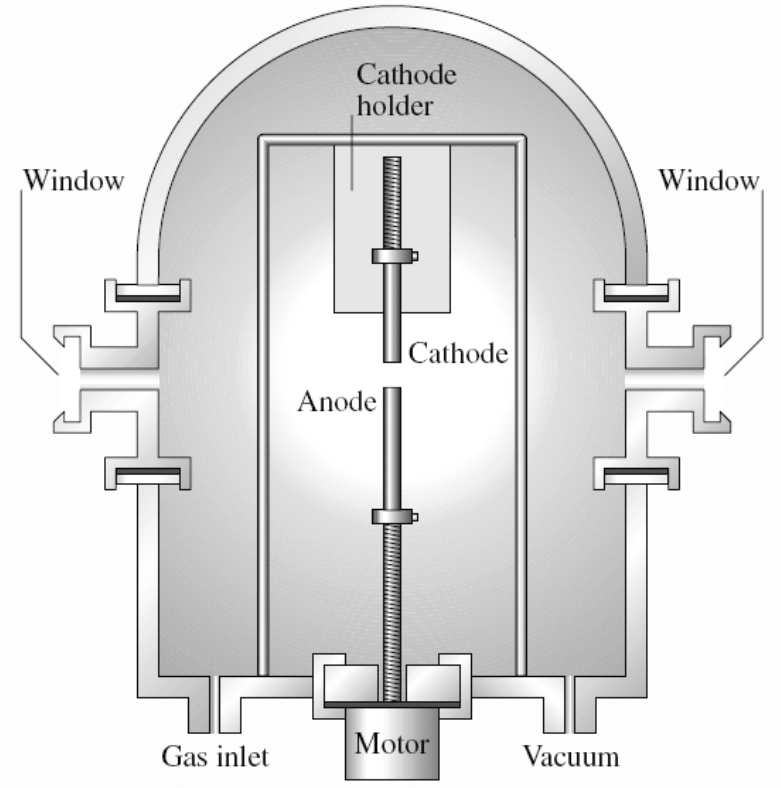

Figure 1.7 Sketch of an electric arc reactor [8].

cobalt as the catalyst. Currently, arc-discharge is the prevailing method to synthesis high quality SWCNTs and MWCNTs.

1.1.3.2 Laser ablation method

Figure 1.8 illustrates an example of the apparatus for making CNTs by laser evaporation method [8]. A quartz tube containing inert gas and a graphite target with the catalyst is placed in a furnace and maintained at a temperature at 1200°C [31] [32]. A water-cooled copper collector is partially contained in the tube. An intense pulsed laser beam is incident on the target, evaporating carbon from the graphite. The inert gas, such as argon, then sweeps the carbon atoms from the high-temperature zone onto the colder copper collector where they condense into nanotubes. MWCNTs with 5-20nm in diameter and tens to hundreds of micrometers in length have been made by this method [31]. In addition to the arc-discharge method, high-quality SWCNTs have also been synthesized by this method [33].

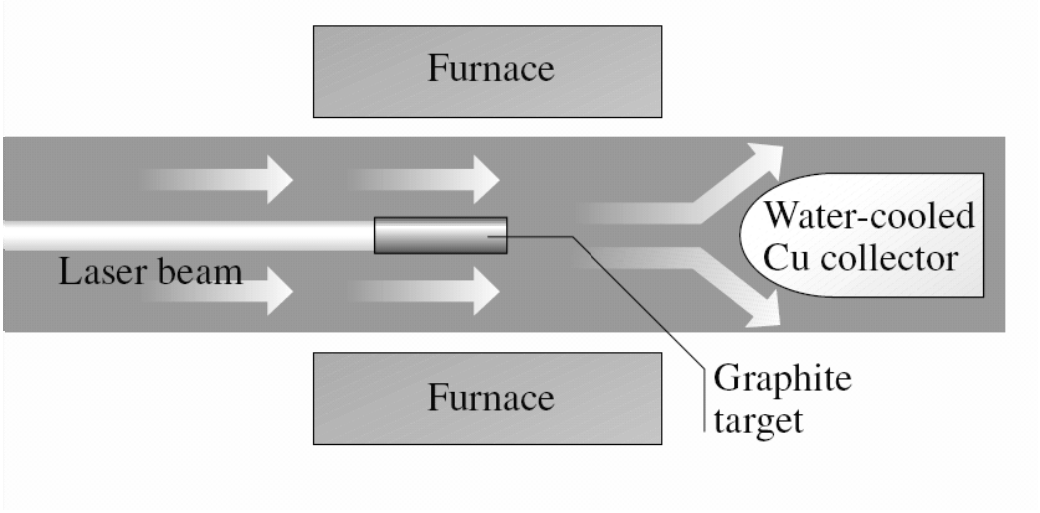

Figure 1.8 Sketch of synthesizing CNTs by a laser vaporization method [8].

1.1.3.3 Catalytic chemical vapor deposition (CCVD)

Catalytic chemical vapor deposition (CCVD) processes are simple and low cost. For this method, substrates with catalysts are placed in the tube furnace and heated up to 500 to 1000ºC [34]-[36]. At this temperature, a continuous flow of hydrocarbon gas (mainly CH_4, C_2H_2, C_2H_4 or C_6H_6, usually as a mixture with either H_2 or an inert gas such as Ar and N_2) is then introduced over a period of time, as demonstrated in Figure 1.9 [8]. The catalyst decomposes the hydrocarbon, releasing hydrogen and carbon, which is free to form nanotubes. The reaction is chemically defined as

$$C_x H_y \rightarrow xC + y/2H_2 \tag{1.4}$$

CNT growth is controlled by many factors, including temperature of the reaction, duration of the treatment, the composition and flow rate of the gas, the form and size of the catalyst, the substrate material and surface morphology. Among those factors, the type of hydrocarbon and catalyst are the most important ones [8]. Catalytic decomposition takes place at the surface of very small size metal particles, typically in nanometer-size range. Due to the low growth temperature, CNTs are formed onto the solid-phase catalyst. Two growth mechanisms are considered to be responsible for

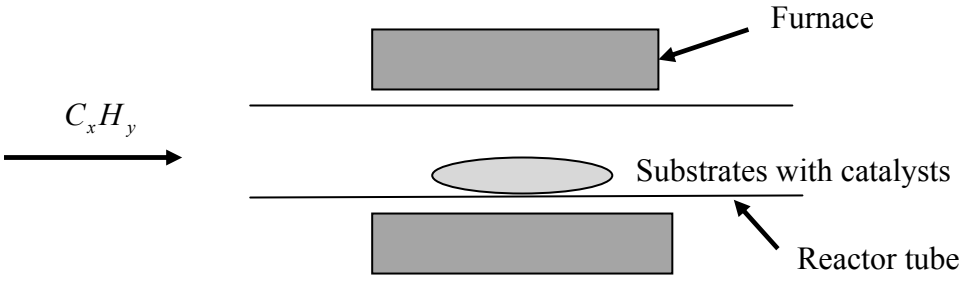

Figure 1.9 Experimental arrangement of synthesizing carbon nanotubes from hydrocarbon gas by catalytic chemical vapor deposition (CCVD) (adapted from [8]).

CNT growth during CCVD: the top-growth and the-base growth models. Figure 1.10 schematically shows these two growth mechanisms. If the catalyst particles stay attached to the surface of the support when carbon dissolves, the CNTs would grow out from the catalyst [34] [36]. This is known as the base-growth model. Contrarily, if the adhesion between the catalyst and the support is too weak to keep the catalyst particles attached to the surface of the support, the nanotubes would form below the catalyst [37] [38]. This growth process is the top-growth model. Both mechanisms have been discussed and the mechanisms differ due to different types of substrate and catalyst used causing different strength of the interaction between the nanoparticles and the support.

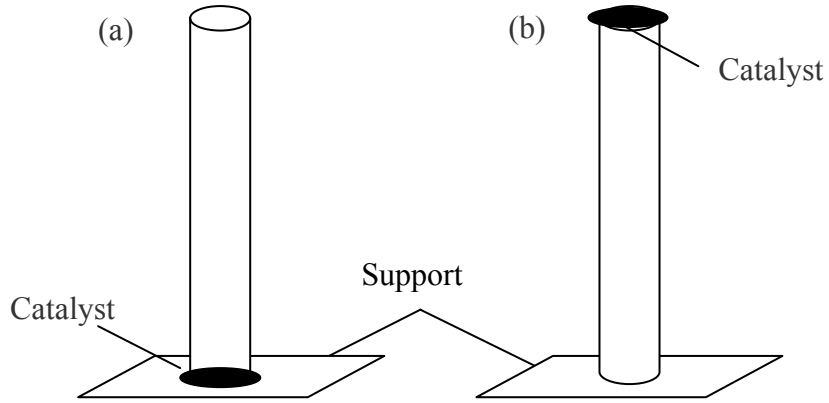

Figure 1.10 Two mechanisms of CNT growth: (a) base-growth (b) top-growth models.

1.1.3.4 Comparison of different CNT growth methods

The advantages of the electric arc-discharge technique lie in the fact that very uniform and almost defect-free nanotubes can be formed during the growing process. The major drawback of this technique is that it is not efficient for large scale production. Both electric arc-discharge and laser ablation techniques are well developed to understand the mechanism of nanotube nucleation and growth. Other disadvantages of these two techniques are the high cost and difficulty to obtain individually separated CNTs. For example, high temperature is required for the CNT growth and undesired tangled-shape CNTs are commonly formed. Though arc-discharge and the laser ablation methods are generally considered not as competitive as the CCVD method in the long term for low-cost production, they are methods currently used to prepare CNTs for commercial products [8]. The CCVD method is considered to be the most favorable method for mass production. Besides its economic advantage, it is the only method of the three that can produce MWCNTs with open end. CCVD technique creates defects, providing lots of C dangling bonds. These dangling bonds are desirable for immobilization of biomolecules.

1.2 Introduction to biosensors

A biosensor is an analytical device which converts a biological response into an electrical signal. Usually, a biological response cannot be examined visually. It has to be converted into a signal which we can easily observe. Figure 1.11 schematically shows how the converting process works. Electrochemical techniques are methods that study reactions at the electrode-solution interface by converting biological responses into signals. In analytical electrochemistry, biocatalyst and transducer constitute a biosensor, which is also considered as an electrode. Transducer is the main component converts the response to measurable electrical signals. Then, the amplifier, processor and display (as analytical electrochemical equipment) convert these signals to visible singles. Reference electrodes are often used to establish a standard that other electrodes may refer.

Biosensors can be classified in many different ways [39]. If sorted according to biocatalyst, biosensors are classified into enzyme electrodes, immunosensors, DNA sensors and microbial sensors. If categorized by transducers, they can be sorted into electrochemical sensors, electrical sensors, optical sensors, mass sensitive sensors and thermal sensors.

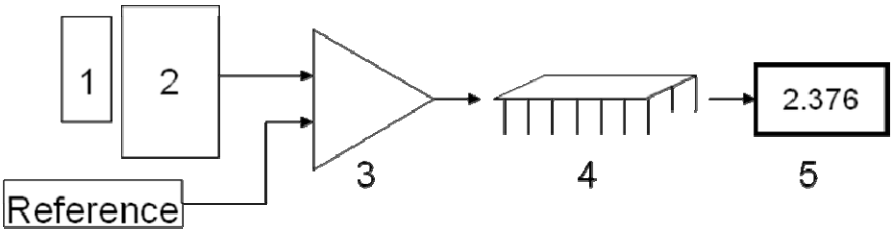

Figure 1.11 Schematic diagram showing a biosensor converts biological response into signals. Five components are: (1) biocatalyst, (2) transducer, (1 and 2 together can be considered as a biosensor) (3)

1.2.1 Glucose biosensors

Glucose plays an important role of the metabolic processes in the human body. Glucose biosensors are devices to be used for determination of glucose level in a biological sample. They are now widely used to test the concentration of glucose for diabetic patients [40].

Glucose biosensors were first described by Clark and Lyons in 1962 [41]. In this design, glucose oxidase (GOx), an enzyme which catalyzes the oxidation of glucose to gluconic acid, was attached to the biosensors. Glucose biosensors are often called

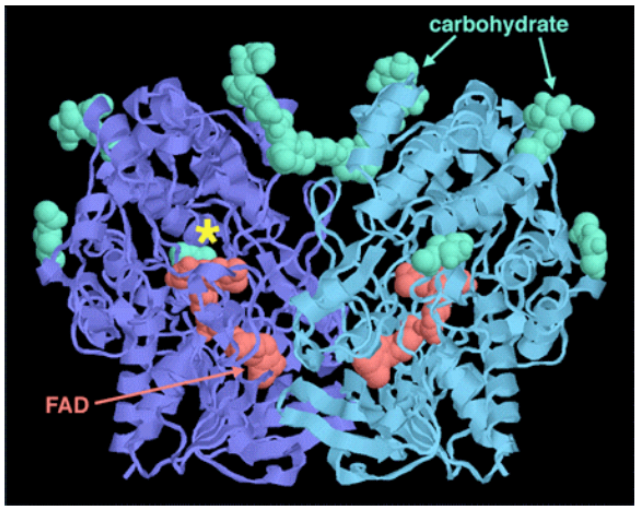

Figure 1.12 Simulated structure of Glucose oxidase (GOx) [43].
FAD is the redox center.

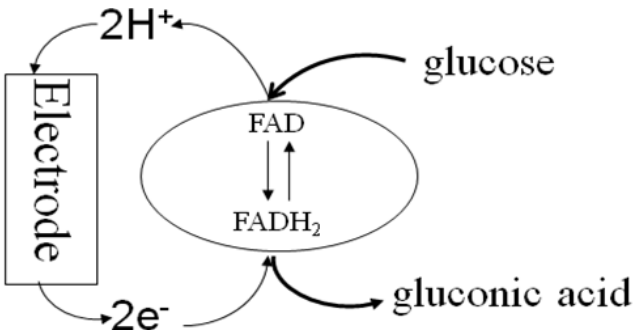

Figure 1.13 Sketch of redox reaction. FAD/$FADH_2$ is the redox reaction center.

enzyme electrodes and have been developed for five decades [42]. One persisting challenge we face today is the establishment of efficient DET between GOx and the electrode surface. Figure 1.13 shows a detailed stimulated structure of GOx molecule [43]. Flavin adenine dinucleotide (FAD, red part in Figure 1.13) is part of GOx structure, where redox (short form of oxidation-reduction) reaction takes place. This FAD/$FADH_2$ redox center is insulated deep inside the protein shell [44]. Thus, the reactive enzyme site is a distance away from the electrode surfaces, as illustrated in Figure 1.12. Then, the main concern for constructing biosensors becomes to establish an efficient DET between the FAD center and the electrode surface.

The early glucose biosensors employed the reduction of glucose by oxygen:

$$\text{glucose} + O_2 \xrightarrow{GOx} \text{gluconic acid} + \text{hydrogen peroxide} \quad (1.5)$$

$$H_2O_2 \rightarrow O_2 + 2H^+ + 2e^- \quad (1.6)$$

One limitation of this method is that errors occur because of the oxygen deficit. The concentration of oxygen is lower than that of glucose by approximately an order of magnitude [42]. To overcome this disadvantage, mediators are used to transfer electrons by the following scheme:

$$\text{glucose} + \text{GOx (FAD)} \rightarrow \text{gluconic acid} + \text{GOx } (FADH_2) \quad (1.7)$$

$$\text{GOx } (FADH_2) + 2M_{(ox)} \rightarrow \text{GOx (FAD)} + 2M_{(red)}^+ + 2e^- \quad (1.8)$$

$$2M_{(red)} \rightarrow 2M_{(ox)} + 2e^- \quad (1.9)$$

where $M_{(ox)}$ and $M_{(red)}$ are the oxidized and reduced forms of the mediator. The electrochemical measurements become basically independent of oxygen by using mediators. One commonly used mediator today is ferrocene or ferricyanide [42].

However, mediator modified electrodes still have limitations due to the leaching problems. Thus a more efficient electron transfer method is needed to overcome this shortcoming.

1.2.2 GOx immobilization

Immobilization is the process of attaching the biological components to the transducer [40]. Figure 1.14 schematically shows the five methods of immobilization: adsorption, covalent bonding, entrapment, microencapsulation, and cross-linking [40] [45]. Among all these methods, adsorption is the simplest and needs minimal preparation. However, the electrodes made by this method can only be used for exploratory work over a short time-span. For the covalent bonding method, covalent bonds between a functional group in the biomaterial and the support matrix need to be carefully designed. The main advantage of this covalent bonding method is that the enzyme will not be released during use. The entrapment method involves the trapping

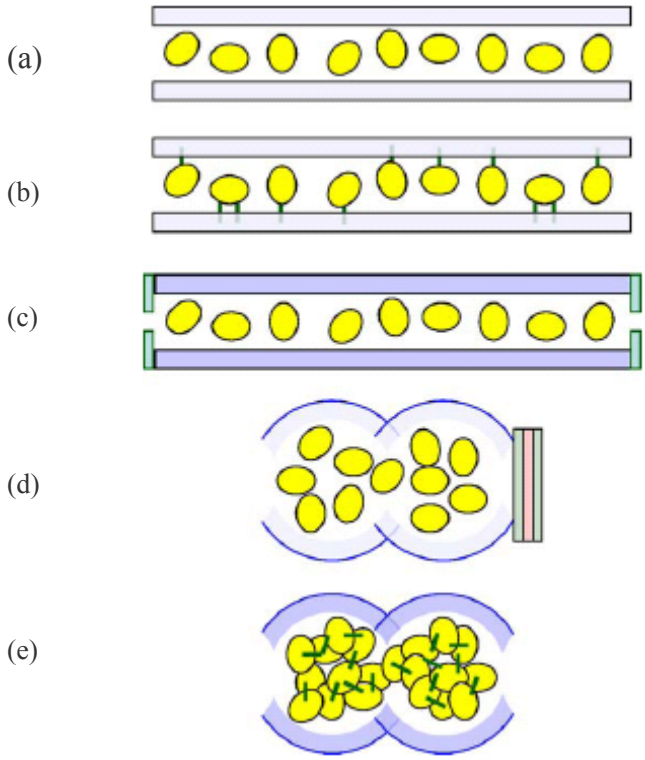

Figure 1.14 Five main methods of immobilization: (a) adsorption, (b) covalent bonding, (c) entrapment, (d) microencapsulation and (e) cross-linking [45].

of the biomaterial in a polymeric gel, which is prepared in a solution containing the biomaterials. Unfortunately, this can cause large barriers, inhibiting the diffusion of substrate and slowing the reaction. Enzyme activity also decreases due to pores in the gel. Microencapsulation is quite adaptable and does not interfere with the reliability of the enzyme. Enabling close contact between the biomaterial and the transducer, the biomaterial is held in place behind a membrane. This method also limits contamination and biodegradation. The cross-linking method bonds the biomaterial to solid supports chemically or to another supporting material such as a gel. Again, diffusion limitation and damages to the biomaterial exist.

In practice, modified electrodes with polymer coatings that facilitate the immobilization of the biocomponents through incorporating multiple immobilization methods are quite common for electrochemical biosensors.

Since GOx serves as the catalyst in the glucose electrolyte, GOx immobilization on the electrodes is essential for the construction of glucose biosensors. As described in section 1.2.1, the redox center of GOx is insulated deep inside the protein shell, so an efficient way to establish the connections between the redox center and the electrode surfaces is highly needed. Among all methods of immobilization, covalent bond is the most desirable one. Functionalized CNTs offer a connection between the FAD redox center and electrode surface by carefully designed covalent bond. Details are discussed in the following section.

1.2.3 CNT-based biosensors

The main advantage of CNTs is their large accessible surface areas due to a high surface-to-volume ratio. This offers possibility of constructing biosensors with high sensitivity. CNT-based electrochemical glucose biosensors have improved the performance of enzyme electrodes dramatically with high sensitivity, fast response and good reversibility [46]-[54].

Functionalized CNTs have been studied to properly immobilize GOx [53]. There are two ways to functionalize CNTs. One approach is to first chemically oxidize the tips or structural defects of the CNTs and then couple them with other molecules via carboxylic, carbonyl and/or hydroxyl groups located at the nanotube tips or its defects. The other method is to directly add the molecules to the graphitic-like surface of the CNTs. For both method, covalent functionalization is of the majority and is associated with the rehybridization of sp^2 bond [8]. Noncovalent functionalization is also possible and has been achieved by wrapping the nanotubes in a polymer [8].

The most commonly used CNT-based glucose biosensors are CNT-coated electrodes [51] . One disadvantage of these CNT-coated biosensors is the insolubility of CNTs in most solvents. The insolubility of CNTs prohibits the electron transfer due to the limited accessible surface. To overcome this shortcoming, Nafion was utilized to dissolve CNTs [46].

Another advantage is that CNTs provide a direct connection between the FAD redox center of GOx and the electrodes. Glucose biosensors based on vertically aligned CNTs have recently received great attention [47] [55]-[57]. Figure 1.15 shows

the schematic diagram of the covalent bonding between the CNTs and the FAD redox center. GOx were immobilized on the sidewalls (Figure 1.15 (a)) and tips (Figure 1.15 (b)) of the CNTs, which offers DET from the FAD center to the electrodes and also keeps the bioactivities of GOx. These vertically aligned nanotubes are well separated, work as individual electrodes and efficiently collect signal [55]. However, these forest-like CNTs are often in bundles, which decrease the accessible surface area.

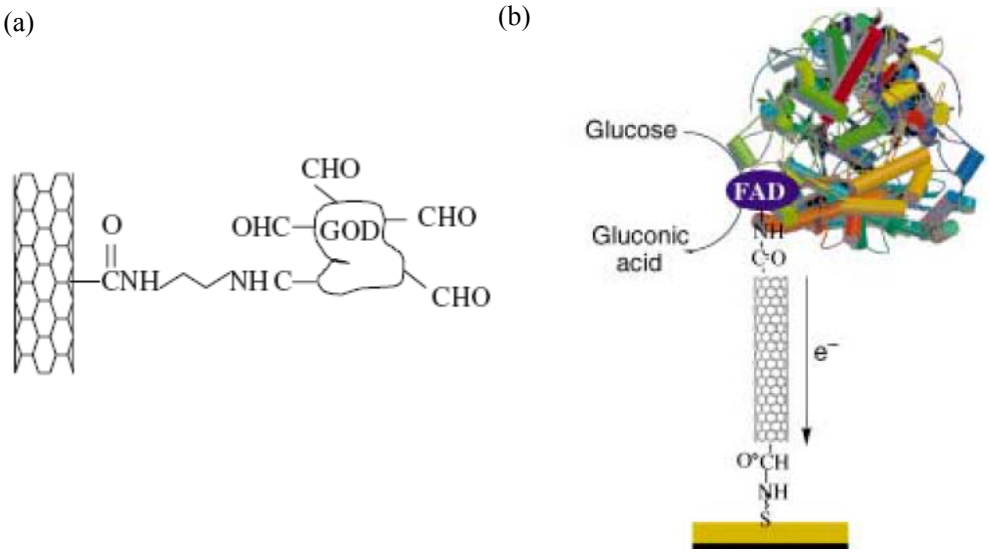

Figure 1.15 Immobilization of GOx via the walls (a) [56] and tips (b) [55] of CNTs.

1.3 Introduction to characterization methods

1.3.1 Characterization of CNTs

To understand properties of CNTs, it is quite necessary to characterize their structure at an atomic level. Various analytic methods have been employed to investigate the structure of nanomaterials. For instance, scanning electron microscope (SEM) and transmission electron microscopy (TEM) are very useful tools for imaging and structure analysis [58] [59]. Among all electron beam instruments, SEM is the most commonly used to obtain nanoscale information from various nanomaterials. High-quality images are obtained with an image resolution of 0.5 nm. TEM determines the atomic structure of interfaces and defects with high position accuracy. The resolution of TEM reaches as high as 0.1nm. Another advantage of electron microscope is that it offers the accessibility of associated spectroscopy and diffraction. For example, SEM and TEM provide quantitative analysis and chemical composition determination when combined with energy dispersive X-ray spectrometry (EDS).

To study the structure of CNTs, the most commonly used to explore the overall structure of CNTs is TEM, which have been used ever since CNTs were discovered [1] [2]. There are other methods that have been used to study the structure of CNTs such as scanning tunneling microscopy (STM) [60] [61], Raman spectroscopy [62]-[64], atomic force microscopy (AFM) [9] and X-ray Diffraction (XRD) [10].

1.3.2 Electrochemical methods

Among all electrochemical methods, cyclic voltammetry is the most widely used technique for acquiring quantitative information about oxidation and reduction (redox) reactions [65] [66]. Cyclic voltammetry studies redox properties of chemicals and interfacial structures. It has the ability to rapidly provide considerable information on the thermodynamics of redox processes and the kinetics of heterogeneous electron transfer reactions and on coupled chemical reactions or adsorption processes. In an electroananlytical study, cyclic voltammetry is often the first experiment performed.

Cyclic voltammetry involves the process of linearly scanning the potential of a stationary working electrode (usually in an unstirred solution), using a triangular potential wave form (Figure 1.16). The working electrode serves as the surface where the electron transfer of the redox reaction occurs. A scale of the potential *E* of the electrode can be established against the standard hydrogen electrode (SHE). Hence, CV is always carried out using a three-electrode system. The SHE is a reference electrode, to which other electrodes may be referred. However, it is not routine to use

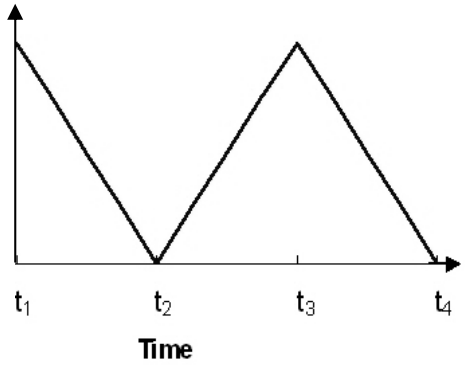

Figure 1.16 Triangular potential in cyclic voltammetry technique (adapted from [66]).

SHE as a reference electrode because it is explosive. Other secondary reference electrodes are used in practice. They give reproducible electrode potentials and have low coefficients of variation with temperature. The silver-silver chloride (Ag/AgCl) electrode and the saturated calomel electrode (SCE) are commonly used ones. The electrodes have potentials of +0.22V and +0.24V relative to SHE, respectively. A counter electrode, also known as an auxiliary electrode is, as well, needed in the electrochemical system.

Single or multiple cycles can be employed to extract information about the electrochemical process. During the potential sweep, the current resulting from the applied potential is measured. The current and potential are then both plotted on a diagram called a cyclic voltammogram. This diagram is a complicated, time-dependent function of a large number of physical and chemical parameters. Figure 1.17 illustrates a typical cyclic voltammogram, presenting the expected

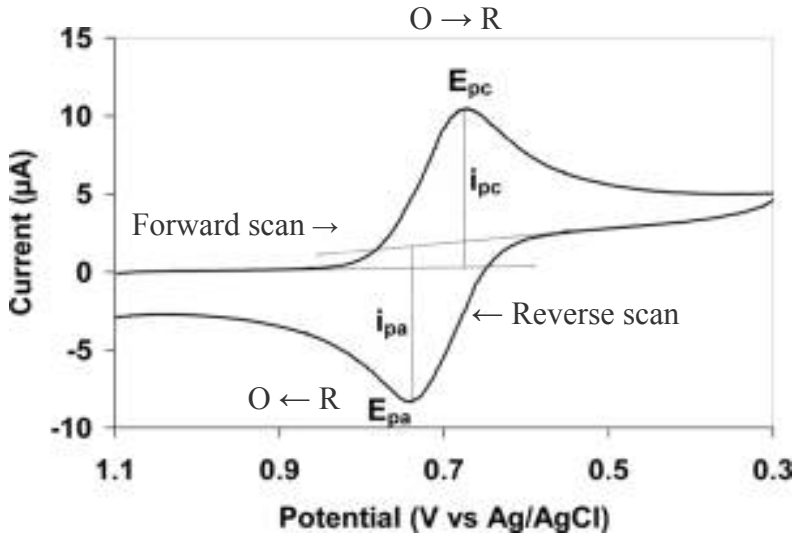

Figure 1.17 Typical cyclic voltammogram, showing one cycle of reversible redox reaction [66].

response of a reversible redox couple during a single potential cycle. The reversible redox reaction is states as:

$$O + ne^- \longleftrightarrow R$$

where O is the oxidized form, R is the reduced form.

The potential increases or decreases linearly as a function of time. When the potential approaches a certain value E^0 during the forward scan, the current begins to increase dramatically, where the reduction process starts. The potential is then reversed at the region that is at least 90/n mV beyond the peak. During the reverse scan, reduced production, generated in the forward half-cycle, is reoxidized back to the oxidized form.

The peak current for a reversible couple (25°C) is given by the Randles-Sevcik equation

$$i_p = (2.69 \times 10^5) n^{3/2} A C D^{1/2} v^{1/2} \tag{1.10}$$

where n is the number of electrons, A the electrode area (in cm^2), C the concentration (in mol/cm^3), D the diffusion coefficient (in cm^2/s), and v the potential scan rate (in V/s).

The reverse-to-forward peak current ratio, $i_{pr}/i_{pf,}$ is 1 for a simple reversible couple. The potential at which the peak occurs, E_p, is related to the standard redox potential E^0, expressed as:

$$E^0 = \frac{E_{pa} + E_{pc}}{2} \tag{1.11}$$

The separation between the peak potentials (for a reversible couple) is given by

$$\Delta E_p = E_{pc} - E_{pa} = \frac{0.059}{n} V \tag{1.12}$$

It is possible to relate the half-peak potential $E_{p/2}$, where the current is half of the peak current, to the polarographic half-wave potential, $E_{1/2}$:

$$E_{p/2} = E_{1/2} \pm \frac{0.056}{n} V \tag{1.13}$$

One of the most common redox reactions used to illustrate a reversible cyclic voltammetric response is the redox between the ferricyanide ion and ferrocyanide:

$$[Fe(CN)_6]^{3-} + e^- \longleftrightarrow [Fe(CN)_6]^{4-} \tag{1.14}$$

If the electrode process is irreversible, the peaks will be reduced in size and widely separated. However, the average of the two peak potentials is still E^0. The peak current, given by

$$i_p = (2.69 \times 10^5) n(\alpha n_a)^{1/2} ACD^{1/2} v^{1/2} \tag{1.15}$$

is still proportional to the bulk concentration, but will be lower in amplitude.

For a quasi-reversible system, the current is controlled by both the charge transfer and mass transport. The voltammogram of a quasi-reversible system exhibits a greater separation in peak potentials compared to a reversible system, but less than an irreversible system.

2. Materials and methods

2.1 Anodized aluminum oxide (AAO) template

Lithography is a conventional technique used to develop controllable pattern of small size. However, it has both technical and economical limitations such as low throughput, long exposure time, small field size and high cost of equipment for large scale integrated fabrication. The template-assisted technique offers a platform that could produce large amounts of nanometer-scaled structures by well patterned nanoarrays, which overcomes the difficulty for conventional lithography. As a commonly used template for filtration, anodized aluminum oxide (AAO) has been well studied over the past half century [67]-[76]. This self-organizing method offers a promising route to synthesizing nanostructures due to AAO's high surface-to-area ratio, controllable pore diameter and ideal cylindrical shape. AAO template pattern provides uniform pore diameter adjustable from 20-200nm, uniform pore periodicity in the range of 50-400nm, and a high packing density of 10^{9}-10^{11} cm^{-2} [68]. The pore diameter, the spacing and the array size varies over ranges that are beyond the reach of standard e-beam lithography. Another advantage of fabrication using AAO

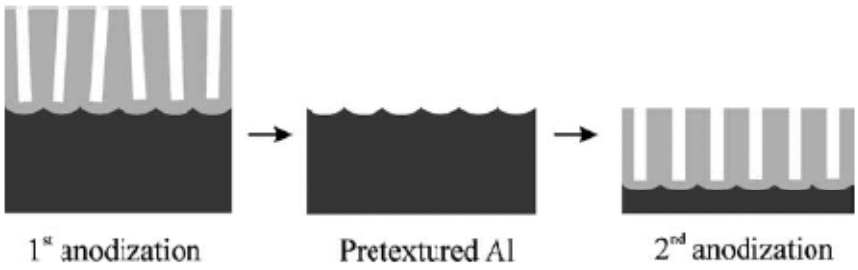

Figure 2.1 Schematic diagram of the two-step anodization process.
(a) first anodization; (b) pretextured Al; (c) second anodization [68].

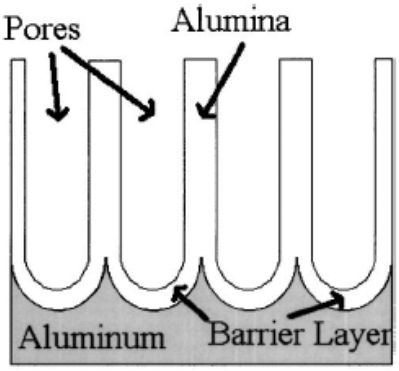

Figure 2.2 Diagram of the typical porous alumina structure
when fabricated using bulk aluminum [73].

templates is the low cost and easy process, compared to other techniques such as a cleanroom process.

Traditional AAO template fabrication with only one-step anodization results in templates with disordered and non-uniform structure. More recently, a two-step anodization process has been well established to achieve self-organized highly-ordered nanopatterns in the AAO template [69] [70]. This carefully controlled two-step anodization process significantly improves the pore regularity. Figure 2.1 shows a schematic diagram of this two-step anodization process. During anodization, the aluminum oxide obtained from the first anodization step is removed and then a porous alumina film with highly ordered pores develops in the second anodization. A barrier layer is formed during anodization as a semi-spherical aluminum oxide layer at pore bottoms [73]. (See Figure 2.2) This undesirable layer is minimized by dropping the voltage at a relative slow speed (1 V/min) after second anodization or removed by etching treatments [74].

The composition of electrolyte, anodization temperature and voltage are the

main factors that affect pore diameter and spacing [71] [75]. Table 2.1 shows the optimized anodization conditions for various electrolytes [76]. Characterization of the morphology of the AAO template surface was obtained by SEM, AFM and XRD. Pore-widening is a simple technique that can modify the pore size of alumina membranes after anodization. This method provides a convenient way to prepare AAO template of any desired diameter in a certain range by chemical etching.

Table 2.1 Optimized anodization conditions for various electrolytes [76]

*E*lectrolyte	*Concentration (M)*	*Temperature (°C)*	*Voltage (V)*	*Typical pore diameter (nm)*
Oxalic acid	0.3	10	40	45
Phosphoric acid	1.0	0	160	400
Sulphuric acid	0.5	0	25	30

The alumina membrane can be separated from the aluminum substrate by wet etching in 1-2wt% HgCl solution [69] [73]. Recently, another method is reported to separate the membrane from Al sheets by voltage pulse [77] [78]. This voltage pulse separation process takes only several minutes, which offers a simple way to obtain free-standing AAO templates.

2.2 Methodology of electrode design

2.2.1 Preliminary electrode design

The object of the research is to develop a general design for biosensors. Glucose biosensor is selected as the model system to verify the design of the biosensors. Figure 2.3 shows the preliminary design of glucose biosensor. In this design, there are four main steps: AAO template fabrication, gold deposition, GOx immobilization and characterization. Porous highly ordered AAO templates are prepared by two-step anodization. Deposited gold on both sides of electrodes surfaces serve as contacts and prevent non-specific adhesion of GOx on the surface. And then GOx is adsorbed to the sidewalls of the porous alumina membrane's nanopores. Electrochemical characterization provides feedback for optimizing the nanostructured electrode device. Cyclic Voltammetry (CV) in $[Fe(CN)_6]^{3-}$ /$[Fe(CN)_6]^{4-}$ system is carried out to determine the minimum thickness of Au coating as effective contact. Finally, study of

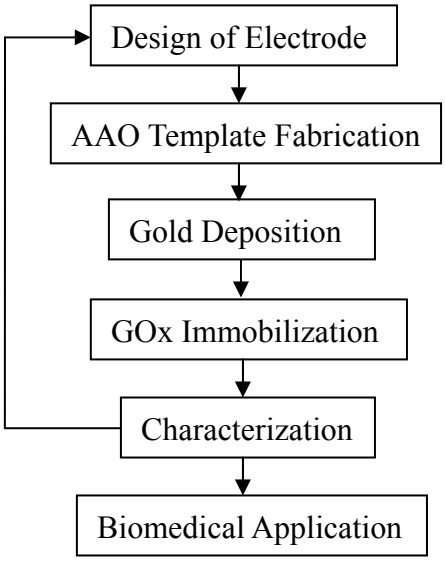

Figure 2.3 Methodology of preliminary electrochemical glucose biosensor design.

enzymatic redox in glucose solutions by CV is attempted.

One method of GOx immobilization is to adsorb several layers of protein nanotubes (known as binding agents) onto the pore of AAO template and then attach the GOx onto each protein layer. In our design, 3-amino propylphosphonic acid (APA) and glutaraldehyde (GA) are used for immobilization, which is adapted from [79].The chemical structure of APA and GA are shown in Figure 2.4. The nanopore alumina template is immersed first into a solution of APA, resulting in attachment (via the phosphonate) of a monolayer of this molecule to the pore walls. The amino groups are then reacted with an excess quantity of the protein-immobilization agent GA [79], leaving unreacted aldehyde groups on the pore walls. The sample is then exposed to a solution of the desired protein, which reacts via free amino sites with the aldehyde groups on the pore wall.

However, no obvious enzymatic redox reaction is detected in the voltammogram. Thus, we are compelled to revise the GOx electrode design by add CNT to enhance the connection between the redox centers in GOx and the Au contacts.

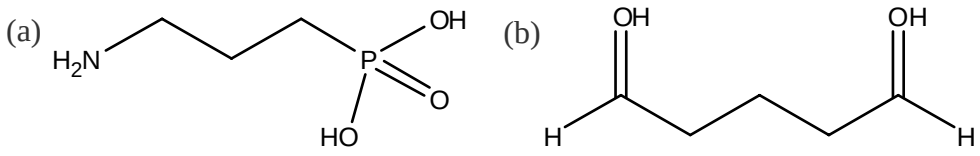

Figure 2.4 Chemical structure of APA (a) and GA (b).

2.2.2 CNT-based electrode design

The flow chart with the major steps involved in the design and construction of CNTs-based glucose electrode is shown in Figure 2.5. To take advantage of the attractive properties of CNTs, the design of enzyme electrodes is modified by adding CNT and immobilizing GOx to the side walls and tips of CNTs. The main difference from the preliminary design is that the step of CNTs fabrication is added after AAO template fabrication and before gold deposition. Figure 2.6 is the schematic diagram of CNT-based electrode fabrication. AAO templates provide vertical, parallel and evenly spacing nanochannels for CNT growth by CCVD method. The templates are then coated with gold on both sides to prevent non-specific protein attachment on the electrode surface and to serve as contacts. A gold wire is attached to the gold surface by conductive tape, which makes the template with gold coating a working electrode.

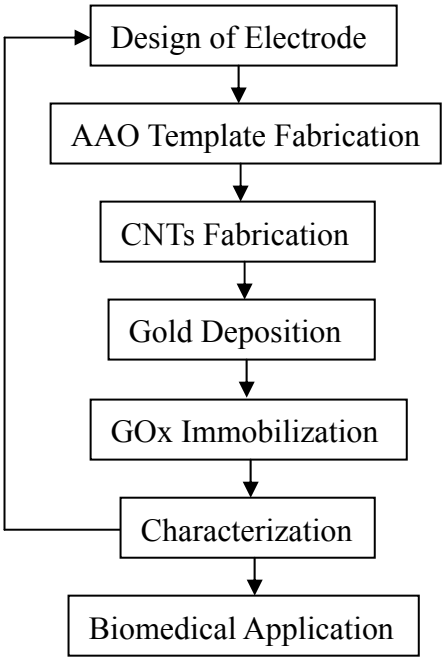

Figure 2.5 Methodology of CNT-based electrochemical glucose biosensor design.

Figure 2.6 (b) shows the GOx immobilization process. Ideally, GOx molecules are immobilized on the side walls and tips of CNTs. For future study, further characterization of this CNT based glucose biosensor by CV and is desirable.

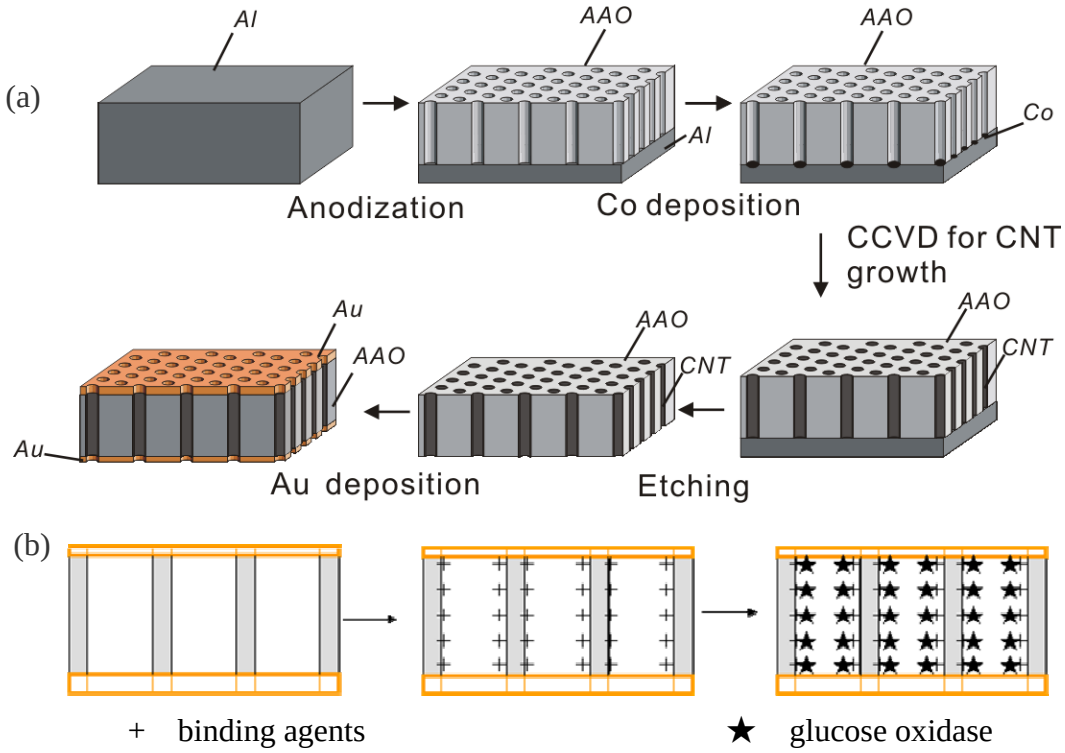

Figure 2.6 Schematic diagrams of CNT-based electrode fabrication (a) and GOx immobilization (b).

3. Experimental

3.1 Preparation of AAO template

High purity (99.999%) aluminum sheets were annealed at 500°C for 4 h. They were polished electrochemically in a chemical solution (C_2H_5O: $HClO_4$ = 5:1) at 20 V (0°C) for 4 min. After the pretreatments, first anodization was carried out at a constant cell potential of 40 V in a 0.3M oxalic acid solution for 16h. Nanopores approximately 60nm in diameter were formed during the first anodization. The porous alumina film was then removed by a chemical etching in a mixture of 6wt% H_3PO_4 1.8wt% CrO_3 in deionized (DI) water for 2 h at 70°C. Subsequently, the Al sheets were anodized again using the same conditions of the first anodization for 5 h. The thickness of alumina membrane increases at the rate of 1micron/15min under these conditions. At the end of the second anodization, the voltage was dropped from 40 to 10V by 1V steps in order to minimize the thickness of the barrier alumina layer at the bottom of the pores, which is of importance to obtain the uniform electrodeposition of the cobalt nanoparticle catalyst. After the pores were widened by immersing the samples in 0.1M H_3PO_4 solution for half an hour, Co was electrochemically deposited at the bottom of the nanopores in $CoSO_4 \cdot 7H_2O$, H_3BO_3, $C_6H_8O_6$ (240:40:1 in weight) electrolyte at 14VAC, 0.1 kHz for 1 min. The samples were rinsed with DI water and dried in the air after each step. Characterization of deposited Co nanoparticles was carried out by using SEM and EDX.

3.2 Study of gold deposition

Two groups of samples were prepared for characterization optimized Au thickness. Group A consisted of two commercial templates purchased from Whatman Company with pore diameter of 200nm and membrane diameter of 13mm. Group B consisted of the empty AAO templates fabricated by two-step anodization in our lab. To remove the barrier layer of the homemade AAO template, the sample was immersed in 0.5M phosphoric acid solution at room temperature for 1 h before Au deposition. 1 wt% $HgCl_2$ solution was used to separate the AAO template from the Al substrate underneath. Gold deposition was carried out to form a continuous coating on both sides for both groups, following the schematic steps shown in Figure 3.1.

For Group A, templates were coated with thickness of 5nm, 20nm or 50nm Au on the front side and 5nm thick Au on the back side using an e-beam evaporator. During the e-beam evaporation, the base pressure was controlled between 4-5x10^{-7} torr and the evaporation rate of 1 Å/s. Gold wires were then attached to the front surfaces of the templates with conductive tape, to form the working electrodes.

CV studies were carried out using a BAS 100 B/W Potentiostat C3 cell in a three-electrode system. The template served as a working electrode, a platinum wire as a counter electrode, and a Ag/AgCl electrode as a reference electrode.

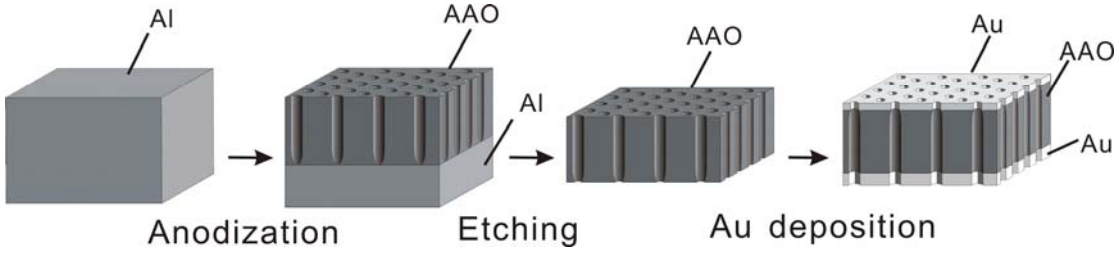

Figure 3.1 Schematic diagram of preparing AAO templates with gold coating.

3.3 Preliminary biosensor construction

The AAO templates with gold coated on both sides were immersed in a 5 mM APA solution at 5.8 pH for 24 hours. Afterwards, the samples were immersed in a 2.5 wt% solution of GA for 12 hours. Finally, the GOx were deposited by vacuum filtration of the 10 mg/mL GOx solution through the membrane, using a Millipore mini-vacuum system. A gold wire was attached to the top of the AAO template by conductive taping.

3.4 Carbon nanotubes growth

CCVD method was applied to grow CNTs in the porous alumina film. To investigate the appropriate conditions for CNT growth by CCVD method, two sets of experiments were carried out. First, empty commercial templates were utilized for CNT growth in pure C_2H_2 gas for 10 minutes, 30 minutes and 1 hour, without catalyst. Thermal cleaning conditions were examined in order to remove junk carbon deposited on the surface of AAO templates. Second, a mixture of 10 vol% acetylene and 90 vol% N_2 has been employed to grow CNTs for 1 h, 2h, 4h and 10 h in home-made AAO templates, using electrodeposited cobalt as a catalyst.

Figure 3.2 shows a schematic of the CNTs growth conditions. The samples, were placed in a tube furnace and were heated up to 600 °C at a rate of 10 °C /min with a flow rate of 60 sccm of pure nitrogen. At 600 °C, N_2 was replaced by pure CO to reduce any cobalt oxides. After 1 hour, the gas was changed to pure acetylene or a mixture gas of 10 vol% acetylene and 90 vol% N_2. In order to find the proper growth time for CNTs, the growth was carried out over different period. After CNT growth, the furnace was cooled down to room temperature in pure N_2 atmosphere.

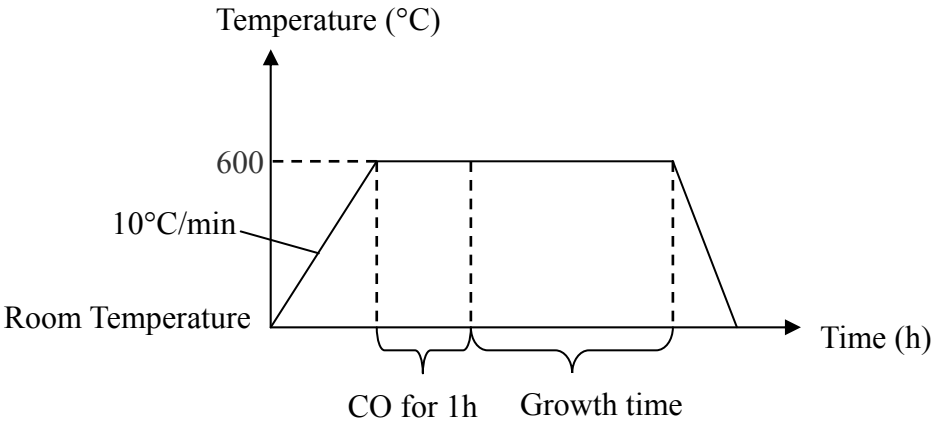

Figure 3.2 Schematic diagram of CNTs growth conditions.

For SEM observation, the AAO template was wet etched in a mixture solution of 6wt% H_3PO_4 and 1.8wt% CrO_3 for 5 hours to partially expose the CNTs. For TEM observation, the CNTs were released by removing the alumina template in 0.5M NaOH solution. The collected CNTs were rinsed by DI water using centrifuge and dispersed in ethanol by sonication. TEM samples were made by dropping a few drops of the ethanol solution containing the CNTs onto copper grids.

4. Results and discussions

4.1 Characterization of AAO templates

The morphology of AAO templates was examined by SEM (JEOL JSM-840). Figure 4.1 shows the top-view and cross-section SEM images of a typical porous alumina membrane fabricated by two-step anodization. A uniform array of nanopores in a hexagonal pattern was obtained. To examine the surface structure of AAO templates, software ImageJ was used to analyze the pore size, spacing and packing density of the templates. Appendix A demonstrates the image analysis details by ImageJ. The average diameter of the nanopores in AAO templates is around 50 nm and the inter-pore distance (distance from the center of one nanopore to the center of a neighboring nanopore) is about 90 nm. The overall packing density is on the order of 10^{10} cm^{-2}. The cross-section SEM image shows that the nanopores are straight and oriented parallel to each other, providing idea nanochannels for one dimensional nanomaterial growth.

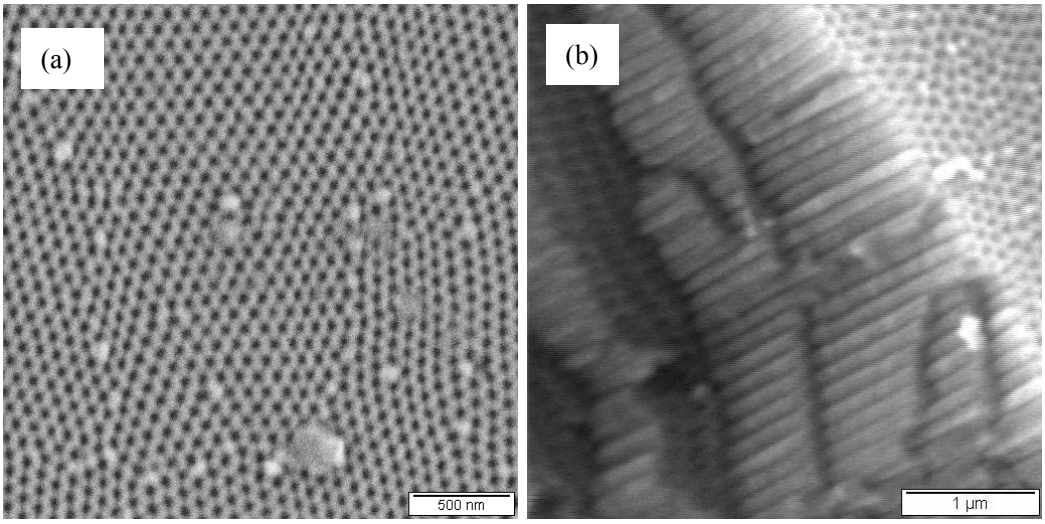

Figure 4.1 Top-view (a) and cross-section (b) SEM images of AAO template after two-step anodization.

In order to facilitate Co catalyst electrodeposition, templates were immersed in 0.1M phosphoric acid solution at room temperature for 30 min to widen the nanopores and thin the barrier layer after the second anodization step. Figure 4.2 shows the top-view SEM image of a typical AAO template after this pore widening treatment. ImageJ analysis indicates that after this pore widening step, the average diameter of the nanopores increased to around 76 nm with a distribution of 6.2%. The nanopore spacing reminded as about 90 nm, confirming that this pore widening treatment does not affect the spacing of nanopores. The details for result analysis by ImageJ are described in Appendix A.

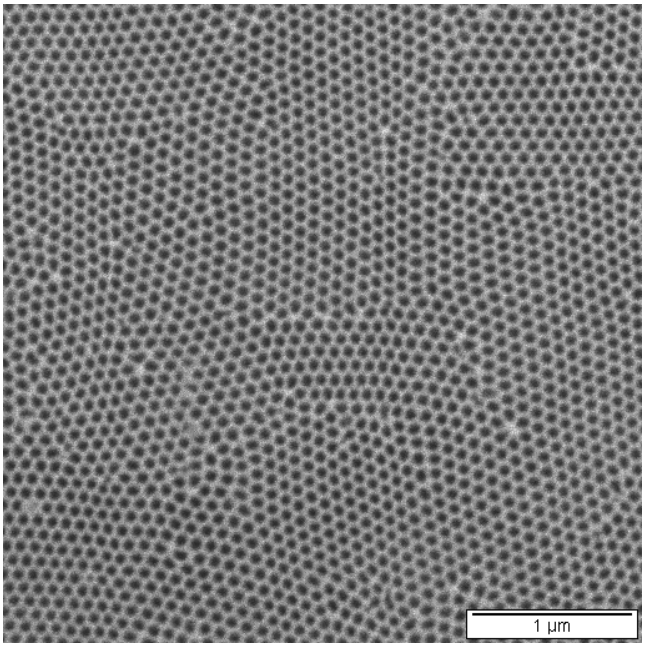

Figure 4.2 Top-view SEM image of AAO template after pore widening.

4.2 Study of Au coating

Cyclic Voltammetry in $[Fe(CN)_6]^{3-}$ /$[Fe(CN)_6]^{4-}$ system was used to test the performance of Au coating as contacts. Figure 4.3 is the cyclic voltammogram of three electrodes with different thickness of gold coating. The electrode with a thickness of 5nm gold coating (sample A1) gets no signal, while the ones with 20nm and 50nm thickness (sample A2 and A3, respectively) obtain electrochemical signals, of which the cyclic voltammogram demonstrated the desired 'duck shape'. The anodic and cathodic peak potentials of sample A2 occur at 164 and 282 mV, and the sample A3 are 182 and 272 mV. The redox potentials for sample A2 and A3 are 0.228 V and 0.227 V respectively, both agree well with the known $[Fe(CN)_6]^{3-}$ /$[Fe(CN)_6]^{4-}$ redox potential relative to Ag/AgCl (0.23 V). The result indicates that 20-50 nm Au coating serves as effective contact to collect electrical signal. In order to enable enzyme

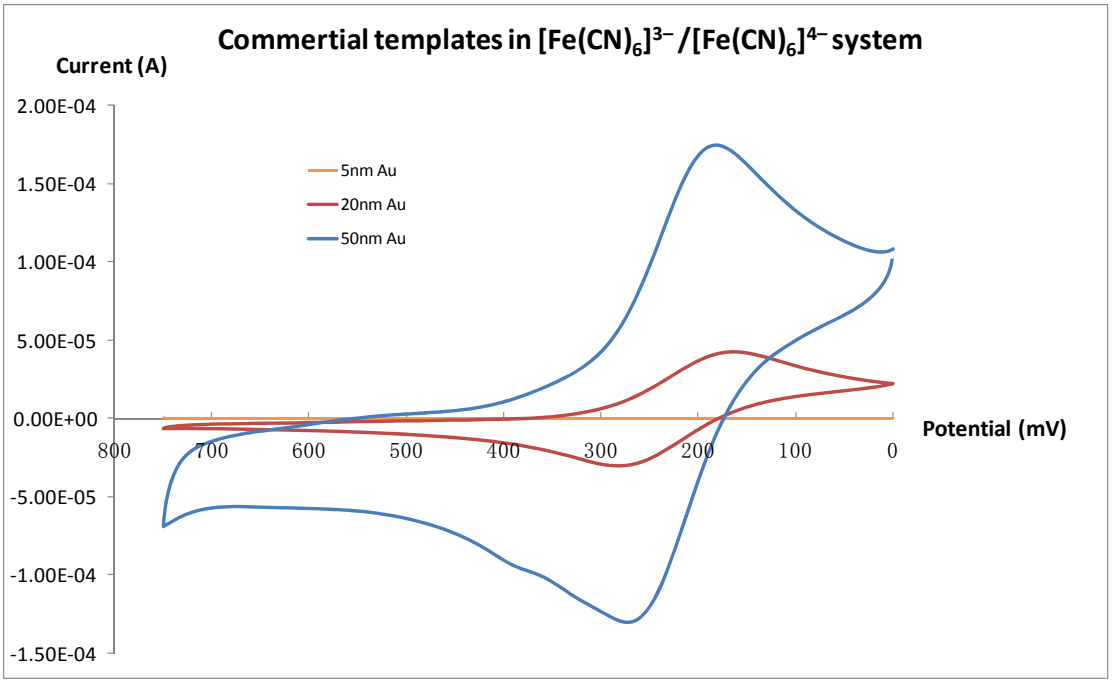

Figure 4.3 Cyclic voltammogram of homemade AAO template with different thickness of gold coating.

attachment to the CNT tips and walls, it is essential that Au coating should be effective to prevent non-specific attachment of enzymes to the AAO surface yet not blocking the openings of the nanopores. Figure 4.4 shows high resolution top-view SEM image of a typical homemade template with 50nm thick gold deposition. Pores with a diameter of ca. 78nm were observed. It indicates that the gold coating does not block the surface, which offers the possibility for accessing CNT for enzyme immobilization.

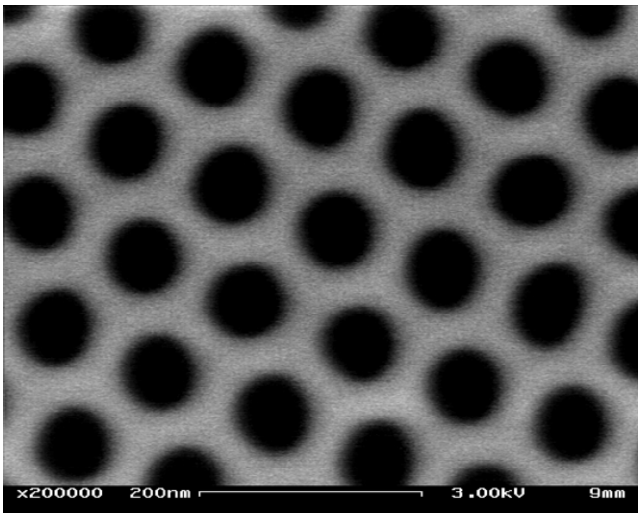

Figure 4.4 Top-view SEM image of empty homemade AAO template with 50nm thickness gold coating.

4.3 Characterization of cobalt deposition

After the cobalt electrodeposition, the samples turned into dark purple. Figure 4.5 (a) shows the top-view SEM image taken after cobalt deposition. It clearly confirms that the opening of the nanopore channels in the AAO template reminded open for further materials deposition. Figure 4.5 (b) is the cross-section SEM image

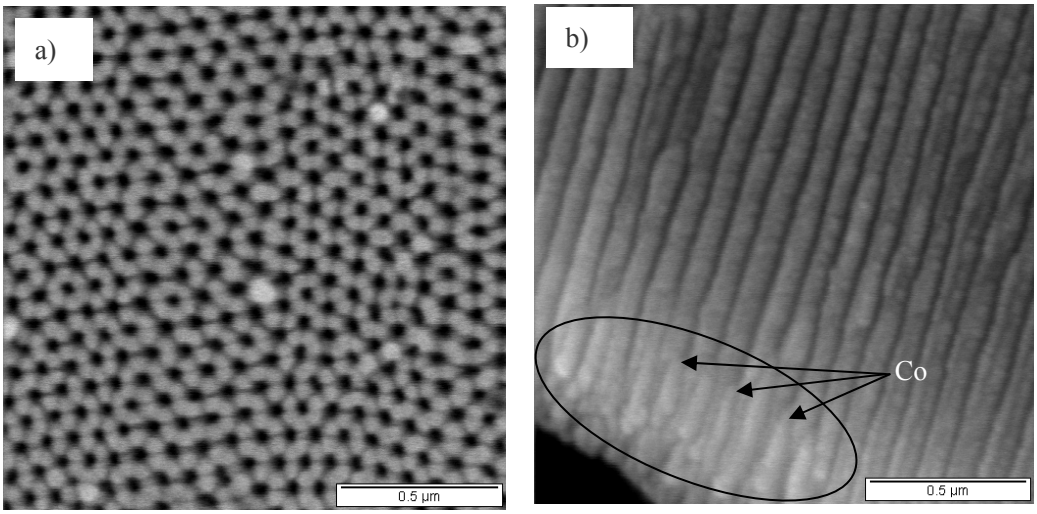

Figure 4.5 Top-view (a) and cross-section (b) SEM images of AAO template after cobalt deposition.

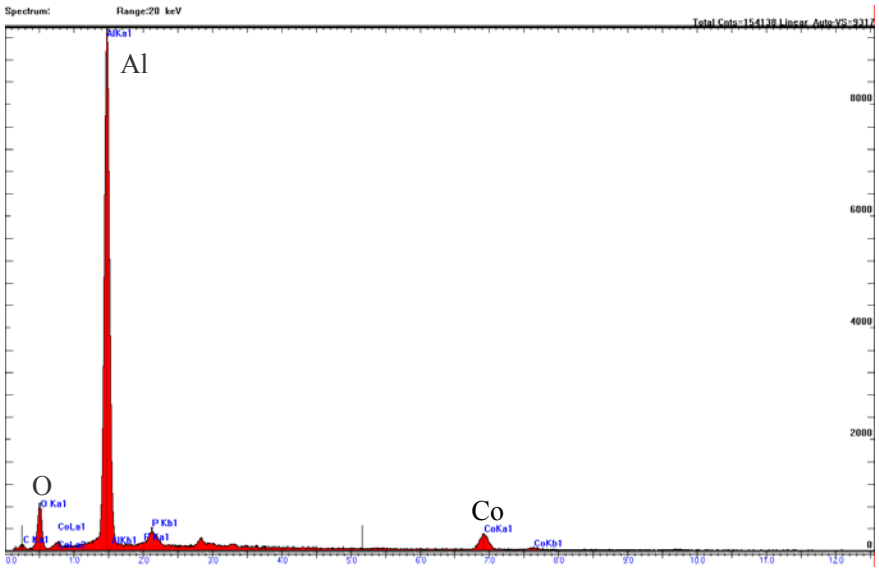

Figure 4.6 Cross-section EDS spectrum of the AAO template after cobalt deposition.

of the AAO template after the cobalt deposition. The electrochemically deposited cobalt formed short nanorods at the bottom of nanochannels in AAO templates. The cross-section EDS spectrum shown in Figure 4.6 confirms the existence of the cobalt. EDS line scan was carried out to characterize the distribution of cobalt along the length of the nanopore. Three different locations on each of three different samples were examined. A representative cross-section SEM image of the AAO template with cobalt deposition and corresponding EDS spectrum line scan along a nanopore from bottom to top are presented in Figure 4.7. The EDS line scan results indicate that the amount of cobalt decreases along the length of the nanopore from bottom to top. Further analysis of SEM cross-section images and EDS line scan results suggests that the average lengths of Co nanorods is around 400nm, as shown in Table 4.1.

Table 4.1 SEM cross-section and EDS line scan results of electrodeposited cobalt length for 1 min

Sample name	*A*				*B*			*C*	
location	1	2	3	4	5	6	7	8	9
Estimated cobalt length (nm)	215	427	507	294	223	498	433	461	683
Average cobalt length (nm)					416				

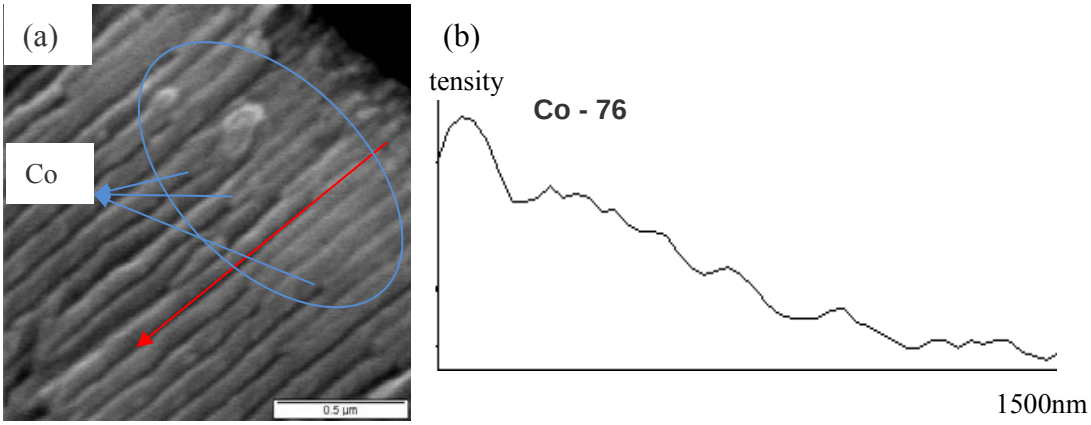

Figure 4.7 Cross-section SEM image of the AAO template after cobalt deposition (a) and EDS spectrum line scan along the length of the nanopore from bottom to top.

4.4 Observation of CNTs

4.3.1 CNT growth in pure C_2H_2

Empty commercial templates were utilized for CNT growth in pure C_2H_2 without any catalyst. Figure 4.8 (a) shows the SEM top-view image of a typical as-grown sample for 1 hour growth. It is obvious that bulk carbon particles of micrometer size were formed on the surface of AAO template. These bulk carbons are known as the junk carbon. In order to remove those junk carbons on the surface, thermal cleaning

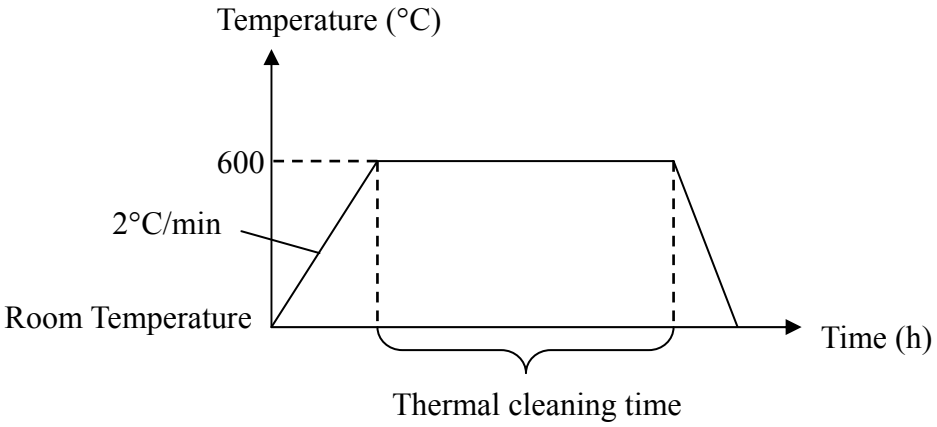

Figure 4.8 Schematic diagram of thermal cleaning.

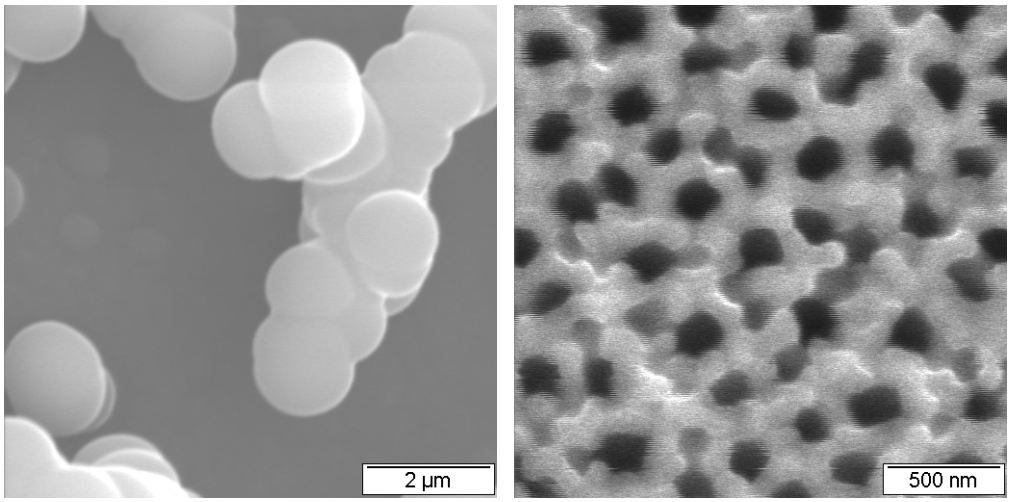

Figure 4.9 Top-view SEM images of commercial AAO templates before (a) and after (b) thermal cleaning.

conditions were studied. The cleaning procedure employed a temperature profile shown in Figure 4.8. The templates were heated to 600°C at 2 °C/min and kept for various periods in air. Three different thermal cleaning periods were tested: 10 min, 30min and 1h. It was found that 1 hour was needed to thoroughly clean the surface with junk carbon. Junk carbon on the AAO surface was removed partially for 10 min or 30 min. Figure 4.9 (b) shows the top-view SEM images of commercial AAO templates after 1 hour thermal cleaning. However, no CNTs were observed after this thermal cleaning process. Even though there were reports suggesting that AAO template can sever as a weak catalyst for CNT CCVD growth [80], under the growth conditions in our study, the catalytic effect might be too weak to result in significant CNT growth. In addition, large size junk carbon might have been formed from the beginning of the growth due to the easy access to the top surface and blocked the passage to the inside of nanopore channels for CNT growth. Thus, a second group of samples were fabricated by employing a mixture of 10 vol% acetylene and 90 vol% N_2 to grow CNTs for 1 h, 2h, 4h and 10 h in home-made AAO templates, using electrodeposited cobalt as catalyst.

4.3.2 CNT growth in C_2H_2 and N_2 mixture gas

CNT growth was performed in a mixture of 10 vol% acetylene and 90 vol% N_2 using electrodeposited Co as catalyst. Figure 4.10 shows the top-view and cross-section SEM images of a typical sample after 1 hour of growth. Very little junk carbon formed on the surface of the AAO templates and the opening of nanopores is clearly visible. From the cross-section view (Figure 4.10 (b)), long tube-like carbon

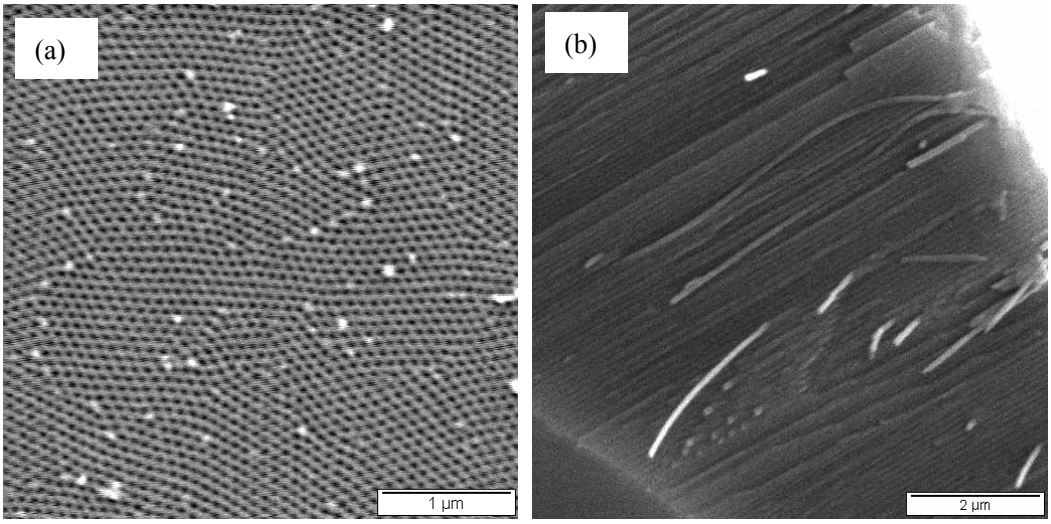

Figure 4.10 (a) Top-view and (b) cross-section SEM images of AAO templates after 1h CNT growth.

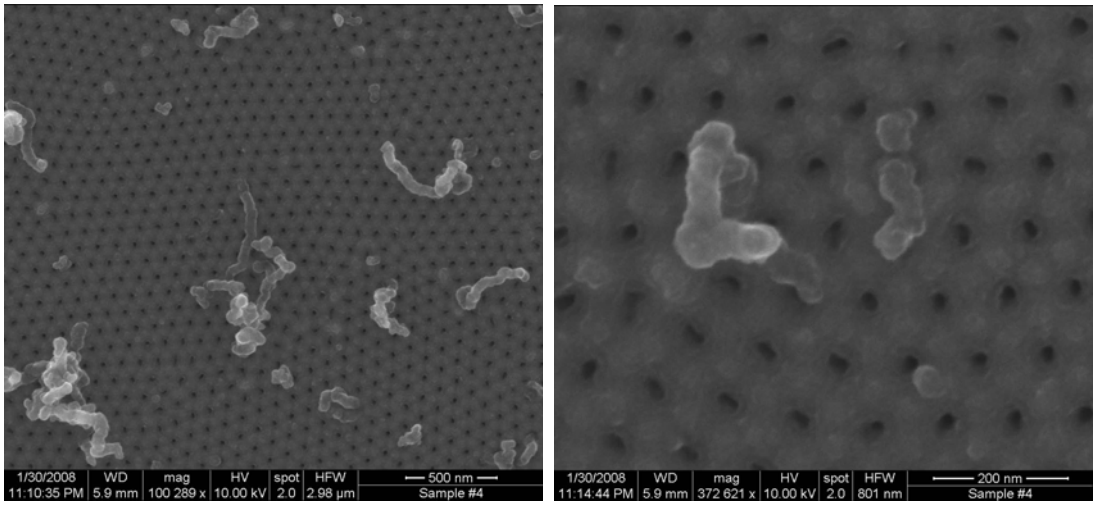

Figure 4.11 High resolution top-view SEM images of AAO templates with CNTs inside nanopores after 5h etching.

was observed.

CNTs in AAO templates were partially exposed by wet etching in a phosphoric acid and chromic acid solution for 5 hours. Figure 4.11 (a) shows the top-view SEM images of a typical sample after this wet etching treatment. Long tube-like structures were seen in Figure 4.11. In the SEM image at high magnification (Figure 4.11 (b)),

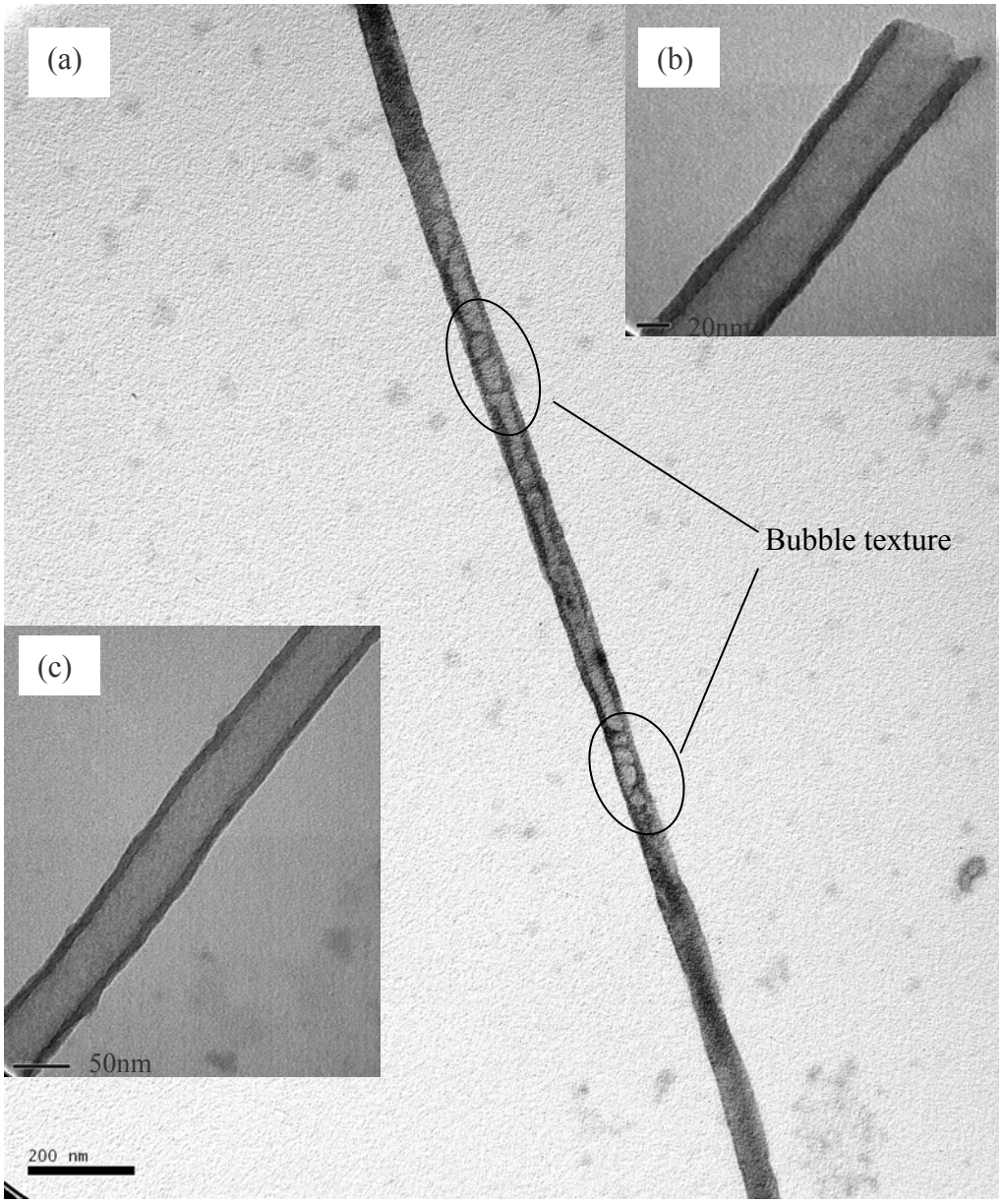

Figure 4.12 TEM images of MWCNT with an open tip (b, c) and bubble texture (a).

in addition to these long tube-like structures, it was observed that shape of the opening of nanopore channels changed to irregular shapes compared with samples without CNT growth (Figure 4.10 (a)) and the diameter of the opening of nanopore channels decreased to 30 nm (analysis by ImageJ) due to the growth of CNTs along the inner wall of nanopore channels. Further CNTs characterization was carried out using TEM (JEOL 100kV TEM). CNTs were released by dissolving the templates in NaOH solution. Figure 4.12 (a) is the TEM image of MWCNT with a hollow shape. Figure 4.12 (b) shows that the tip of as fabricated MWCNTs is open. Figure 4.12 shows that the diameter of the MWCNTs is around 60nm, which agrees with the diameter of the pore size of the AAO template. The length of MWCNTs varies up to the micron scale.

CNTs were synthesized for three other different growth times: 2 h, 4 h and10 h. We can see from the top-view SEM images in Figure 4.13 that more junk carbon was formed on the surface of the templates, compared with 1 h CNT growth, especially for the 10 h growth procedure. After 2 h growth, the surface was relatively clean and nanopores are still visible (Shown in Figure 4.13 (a)). However, after 10 hour of growth,

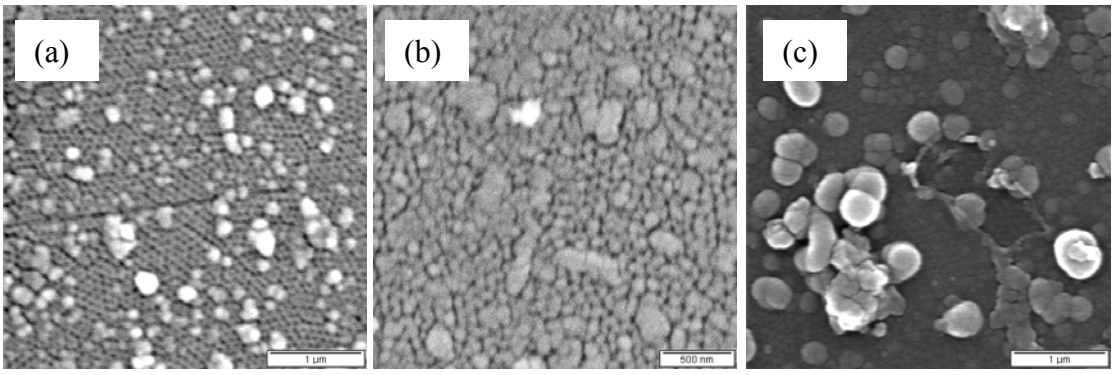

Figure 4.13 Top-view SEM images of AAO template after 2h (a), 4h (b) and 10h (c) CNT growth.

only large carbon particles can be resolved by top-view SEM observation. It was confirmed that the thermal cleaning procedure we developed were effective to remove those large carbon particles, as shown in Figure 4.14, For thermal cleaning, the samples were heated at a speed of 2 °C/min to 600°C and kept for 1 hour in air. Figure 4.15 shows cross-section SEM image of homemade AAO template for 4 h CNT growth. Tube-like carbon was also observed.

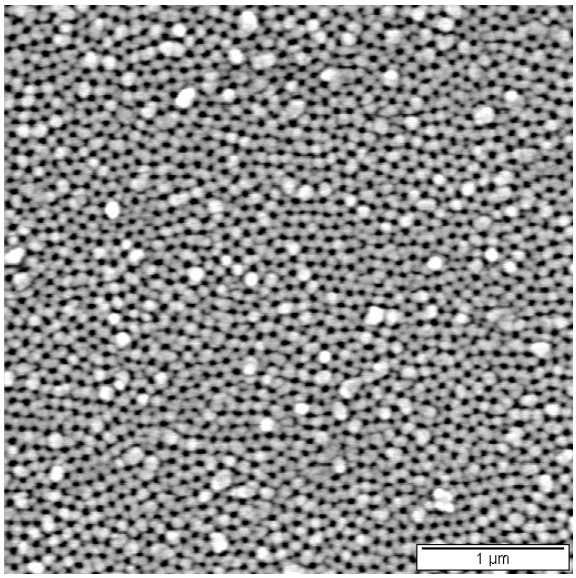

Figure 4.14 Top-view SEM image of homemade AAO template after thermal cleaning procedure for 2 h CNT growth.

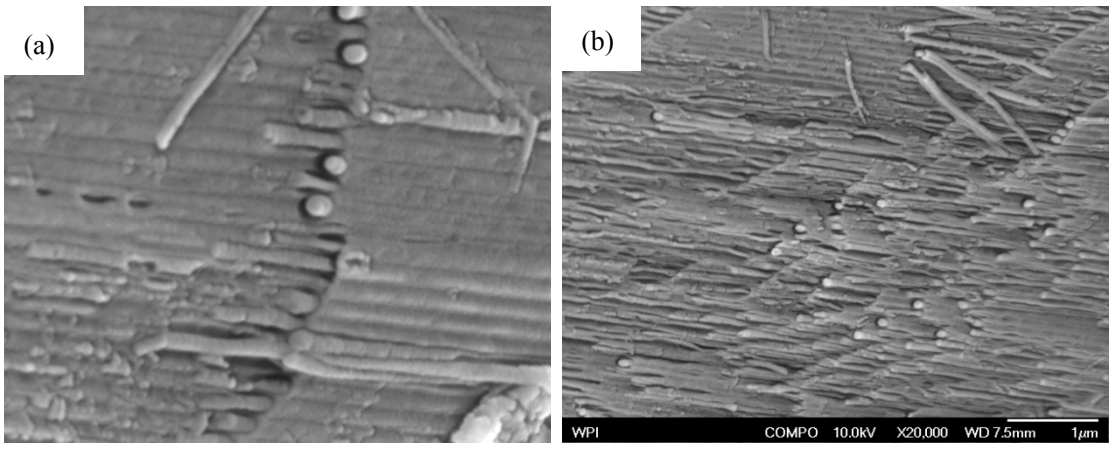

Figure 4.15 Cross-section SEM image of homemade AAO template for 4 h CNT growth.

5. Conclusions

A general design of electrochemical biosensors based on vertically aligned CNTs arrays has been developed. Electrochemically deposited Co was employed as the catalyst to facilitate the CNT growth. MWCNTs with open tips were successfully fabricated by catalytic chemical vapor deposition. The fabricated MWCNTs were characterized using SEM and TEM. CV testing in both $[Fe(CN)_6]^{3-}$ /$[Fe(CN)_6]^{4-}$ system and glucose system show the redox reactions have been observed. Gold deposition of 20nm thickness on the surface of AAO was confirmed to be sufficient to provide effective contact for electrochemical measurements.

6. Future work

Our success in well aligned CNT growth by CCVD and preliminary work on constructing nanostructured biosensors provided unique opportunities for further study of:

1. The growth mechanisms of CNT by CCVD;
2. Highly controllable immobilization of GOx on well-aligned CNT arrays;
3. Synthesis of ultrasensitive glucose nanobiosensor;
4. Electrochemical behaviors of this novel glucose nanobiosensors by CV;
5. Immobilization of other biomolecules such as enzymes on well-aligned CNT;
6. Synthesis and electrochemical characterization of nanobiosensors;
7. The general design of the nanobiosensors based on vertically aligned CNT arrays.

7. References

[1]. Iijima, S. *Nature* **1991***, 354*, 56-8.

[2]. Iijima, S.; Ichihashi, T. *Nature* **1993***, 363*, 603.

[3]. Bethune, D. S.; Klang, C. H.; de Vries, M. S.; Gorman, G.; Savoy, R.; Vazquez, J.; Beyers, R. *Nature* **1993***, 363*, 605.

[4]. Dresselhaus, M. S.; Dresselhaus, G.; Hofmann, M. *Vib. Spectrosc.* **2007**, *45*, 71-81.

[5]. Martel, R.; Schmidt, T.; Shea, H. R.; Hertel, T.; Avouris, P., *Applied Physics Letters* **1998**, *73*, 2447.

[6]. Cheung, C. L.; Hafner, J. H.; Lieber, C. M. *Proc. Natl. Acad. Sci. U.S.A.* **2000**, *79*, 3809-13.

[7]. Wong, S. S.; Joselevich, E.; Woolley, A. T.; Cheung, C. L.; Lieber, C. M. *Nature* **1998**, *394*, 52-5.

[8]. Bhushan, B., Ed. *Springer handbook of nanotechnology* New York: Spinger-Verlag Berlin Heidelberg, **2003**.

[9]. Tsang , S.; de Oliveira, P.; Davis, J. J.; Green, M. L. H.; Hill, H. A. O. *Chem. Phys. Lett.* **1996***, 249*, 413-22.

[10]. Monthioux, M.; Smith, B. W.; Vurteaux, B.; Claye, A.; Fischer, J. E.; Luzzi, D. E.; *Carbon* **2001***, 39*, 1251-72.

[11]. Ebbesen, T. W.; Ajayan, P. M. *Nature* **1992***, 358*, 220-2.

[12]. Saito, R.; Fujita, M.; Dresselhaus, G.; Dresselhaus, *Appl. Phys. Lett.* **1992***, 60*, 2204.

[13]. Hamada, N.; Sawada, S.; Oshiyama, A. *Phys. Rev. Lett.* **1992***, 68*, 1579-81.

[14]. Wildoer, J. W. G.; Venema, L. C.; Rinzier, A. G.; Smalley, R. E.; Dekker, C. *Nature* **1998**, *391*, 59.

[15]. Odom, T. W.; Huang, J.-L.; Kim, P.; Lieber, C. M. *Nature* **1998**, *391*, 62.

[16]. Poole Jr., C. P.; Owens, F. J. *Introduction to Nanotechnology* Hoboken: John Wiley & Sons, Inc. **2003**.

[17]. Berber, S.; Kwon, Y.; Tomanek, D. *Phys. Rev. Lett.* **2002**, *84*, 4613-6.

[18]. Baughman, R. H.; Zakhidov, A. A.; de Heer, W. A. *Science* **2002**, *297*, 787-92.

[19]. Yu, M.; Lourie, O.; Dyer, M. J.; Moloni, K.; Kelly, T. F.; Ruoff, R. S. *Science* **2000***, 287*, 637-40.

[20]. Walters, D. A.; Ericson, L. M.; Casavant, M. J.; Liu, J.; Colbert, D. T.; Smith, K. A.; Smalley, R. E. *Appl. Phys. Lett.* **1999***, 74*, 3803-5.

[21]. Yakobson, B. I.; Brabec, C. J.; Bernholc, J. *Phys. Rev. Lett.* **1996***, 76*, 2511-4.

[22]. Wong, E. W.; Sheehan, P. E.; Lieber, C. M. *Science* **1997***, 277*, 1971-5.

[23]. Gao, R.; Wang, Z. L.; Bai, Z.; de Heer, W. A.; Dai, L.; Gao, M. *Phys. Rev. Lett.* **2000***, 85*, 622-5.

[24]. Zhao, J.; Buldum, A.; Han, J.; Ping Lu, J. *Phys. Rev. Lett.* **2000**, *85*, 1706-9.

[25]. Cadek, M.; Coleman, J. N.; Barron, V. *Appl. Phys. Lett.* **2002**, *81*, 5123-5.

[26]. Tasca, F.; Gorton, L.; Wagner, J. B.; Nöll, G. *Biosens. Bioelectron.* **2008**, *24*, 272-8.

[27]. Cheung, C. L.; Hafner, J. H.; Odom, T. W.; Kim, K.; Lieber, C. M. *Appl. Phys. Lett.* **2000**, *76*, 3136-8.

[28]. Bianco, A.; Kostarelos, K.; Prato, M. *Curr. Opin. Chem. Biol.* **2005**, *9*, 674-9.

[29]. Zhao, Q.; Gan, Z.; Zhuang, Q. *Electroanalysis* **2002**, *14*, 1609-13.

[30]. Wei, T.; Fan, Z.; Luo, G.; Wei, F.; Zhao, D.; Fan, J. *Mater. Res. Bull.* **2008**, *43*, 2806-9.

[31]. Guo, T.; Nikolaev, P.; Rinzler, A. G.; Tomanek, D.; Colbert, D. T.; Smalley, R. E. *Chem. Phys. Lett.* **1995***, 99*, 10694-7.

[32]. Guo, T.; Nikolaev, P.; Thess, A.; Colbert, D. T.; Smalley, R. E. *Chem. Phys. Lett.* **1995**, *243*, 49-54.

[33]. Thess, A.; Lee, R.; Nikolaev, P.; Dai, H.; Petit, P.; Robert, J.; Xu, C.; Lee, Y. H.; Kim, S. G.; Rinzler, A. G.; Colbert, D. T.; Scuseria, G. E.; Tománek, D.; Fischer, J. E. and Smalley; R. E. *Science* **1996**, *273*, 483.

[34]. Li, J.; Papadopoulos, C.; Xu, J. M.; Moskovits, M. *Appl. Phys. Lett.* **1999***, 75*, 367-9.

[35]. Yuan, Z.; Huang, H.; Liu, L.; Fan, S. *Chem. Phys. Lett.* **2001**, *345*, 39-43.

[36]. Kong, J.; Cassel, A. M.; Dai, H. *Chem. Phys. Lett.* **1998**, *292*, 567-74.

[37]. Lee, J. S.; Gu, G. H.; Kim, H.; Jeong, K. S.; Bae, J.; Suh, J. *Chem. Mater.*, **2001**, *13*, 2387-91

[38]. Yun, Y.; Shanov, V.; Tu, Y.; Subramaniam, S.; Schulz, M. J. *J. Phys. Chem. B* **2006**, *110*, 23920-5.

[39]. Cass, A. E. G. *Biosensors: A Practical Approach* Oxford: IRL Press, **1990**.

[40]. Eggins, Brian *Biosensors: An Introduction*, Teubner: John Wiley & Sons, Ltd and B. G. **2006**.

[41]. Clark, L. C.; Lyons, C. *Ann. N. Y. Acad. Sci.* **1962***, 102*, 29.

[42]. Wang, J. *Electroanalysis* **2001**, *13*, 983-8.

[43]. Goodsell, D. S. *Molecule of the Month* **2006**. http://www.rcsb.org/pdb/static.do?p=education_discussion/molecule_of_the_month/molecule_list_2006.html

[44]. Degani, Y.; Heller, A. *J. Phys. Chem.* **1987**, *91*, 1285-9.

[45]. Kim, J.; Jia, H.; Wang, P. *Biotech. Adv.*, **2006**, *24*, 296-308.

[46]. Wang, J.; Musameh, M.; Lin, Y. *J. Am. Chem. Soc.* **2003**, *125*, 2408-9.

[47]. Lin, Y.; Lu, F.; Tu, Y.; Ren, Z. *Nano Lett.* **2004**, *4*, 191-5.

[48]. Zou, Y.; Xiang, C.; Sun, L.; Xu, F. *Electrochim. Acta* **2008**, *53*, 4089-95.

[49]. Cao, Z.; Jiang, X.; Xie, Q.; Yao, S. *Biosens. Bioelectron.* **2008**, *24*, 222-7.

[50]. Wu, B.; Hou, S.; Yu, M.; Qin, X.; Li, S.; Chen, Q. *DNLM*, **2008**, *In Press.*

[51]. Wang, J. *Electroanalysis* **2005**, *17*, 7-14.

[52]. Vamvakakl, V.; Tsagarakl, K.; Chanlotakls, N. *Anal. Chem.* **2006** *78*, 5538-42.

[53]. Withey, G. D.; Lazareck, A. D.; Tzolov, M. B.; Yin, A.; Aich, P.; Yeh, J. I.; Xu, J. M. *Biosens. Bioelectron.* **2006**, *21*, 1560-5.

[54]. Gouveia-Caridade, C.; Pauliukaite, R.; Brett, C. M. A. *Electrochim. Acta* **2008**, *53*, 6732-9.

[55]. Patolsky, F.; Weizmann, Y. and Willner, I. *Angew. Chem. Int. Ed.* **2004**, *43*, 2113.

[56]. Li, J.; Wang, Y.; Qiu, J.; Sun, D.; Xia, X. *Anal. Bioanal. Chem.* **2005**, *383*, 918-22.

[57]. Signore, M. A.; Rizzo, A.; Rossi, R.; Piscopiello, E.; Luccio, T. D.; Capodieci, L.; Dikonimos, T.; Giorgi, R. *Diamond Relat. Mater.* **2008**, *In Press.*

[58]. Newbury, D. E.; Williams, D. B. *Acta. Mater.* **2000**, *48*, 323-46.

[59]. Wang, Z. L., Ed. *Characterization of Nanophase Materials* Weinheim: WILEY-VCH Verlag GmbH, **2000.**

[60]. Ge, M.; Sattler, K. *Appl. Phys. Lett.* **1994***, 65*, 2284-6.

[61]. Zhang, Z.; Lieber, C. M. *Appl. Phys. Lett.* **1993***, 62*, 2792-4.

[62]. Rao, A. M.; Eklund, P. C.; Bandow, S.; Thess, A.; Smalley, R. E. *Nature 1950* **1997***, 388*, 257-9.

[63]. Dresselhaus, M. S.; Dresselhaus, G.; Satio, R. Jorio, A. *Phys. Rep.* **2005**, *409*, 47-99.

[64]. Dresselhaus, M. S.; Villalpando-Paez, F.; Samsonidze, G. G.; Chou, S. G.; Dresselhaus, G.; Jiang, J.; Saito, R.; Souza Filho, A. G.; Jorio, A.; Endo, M.; Kim, Y. -A.; *Physica. E* **2007***, 37*, 81-7.

[65]. Wang, J. *Analytical electrochemistry 3rd ed.*, Hoboken: John Wiley & Sons, Inc. **2006**.

[66]. Bard, A.J.; Faulkner, L.R. *Electrochemical Methods: Fundamentals and Applications.* New York: John Wiley & Sons, 2nd Edition, **2000**.

[67]. Anton, A. H.; Sayre, D. F. *J. Pharmacol. Exp. Ther.* **1962**, *138*, 360-75.

[68]. Chik, H.; Xu, J. M. *Mater. Sci. Eng. R Rep.* **2004***, 43*, 103-36.

[69]. Masuda, H.; Fukuda, K. *Science* **1995***, 268*, 1466-8.

[70]. Masuda, H.; Yamada, H.; Satoh, M.; Asoh, H.; Nakao, M.; Tamamura, T. *Appl. Phys. Lett.* **1997***, 71*, 2770-2.

[71]. Li, A. P.; Müller, F.; Birner, A.; Nielsch, K.; Gösele, U. *J. Appl. Phys.* **1998***, 84*, 6023-6.

[72]. Jessensky, O.; Müller, F.; Gösele, U. *J. Electrochem. Soc.* **1998**, *145*, 3735-40.

[73]. Crouse, D.; Lo, Y.; Miller, A. E.; Croue, M. *Appl. Phys. Lett.* **2000**, *76*, 49-51.

[74]. Liang, J.; Chik, H.; Yin, A.; Xu, J. *J. Appl. Phys.* **2001**, *91*, 2544-6.

[75]. Wang, X.; Han, G. *Microelectronic Engineering* **2003***, 66*, 166-70.

[76]. Liang, J.; Chik, H.; Xu, J. *IEEE J Quantum Electron*, **2005**, *8*, 998-1008.

[77]. Yuan, J. H.; He, F. H.; Sun, D. C.; Xia, X. H. *Chem. Mater.* **2004**, *16*, 1841-4.

[78]. Zhao, S.; Chan, K.; Yelon, A.; Veres, T. *Nanotechnology*, **2007**, *18*, 245304-8.

[79]. Hou, S.; Wang, J.; Martin, C. R. *Nano Lett.* **2005**, *5*, 231-4.

[80]. Kyotani, T.; Tsai, L.; Tomita, A. *Chem. Mater.* **1996**, *8*, 2109-13.

APPENDIX

ImageJ is a public domain, Java-based image processing program. It has been widely used to display, edit, process and analyze 8-bit, 16-bit and 32-bit images. In this appendix, ImageJ was used to analyze the pore size, spacing and packing density of the templates, measure the average length of electrodeposited cobalt and determine the length and diameter of CNTs from SEM and TEM images.

In Appendix A, I will demonstrate one example of image analysis in detail by using Figure 4.2 (Top-view SEM image of AAO template after pore widening). Other results obtained by ImageJ are shown in Appendix B.

Appendix A Demonstrated image analysis by ImageJ software

First, open the software ImageJ. Fig. A1 shows the software window. Then open the file that needs to be analyzed in ImageJ. This image will be opened in another window.

The next step is using the scale bar at the bottom part of the image to set scale. In the tool bar, choose straight line tool (See Fig. A1). Draw a line along the scale bar (See Fig. A2). Under menu **Analyze**, choose **Set Scale**. In the open window, put in the known distance and unit of length indicated in the scale bar and then press OK (See

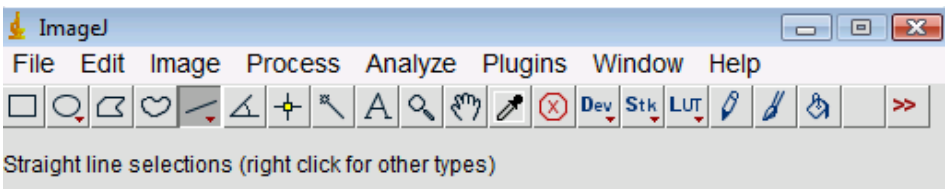

Fig. A1 Tool bar of ImageJ

Fig. A2).

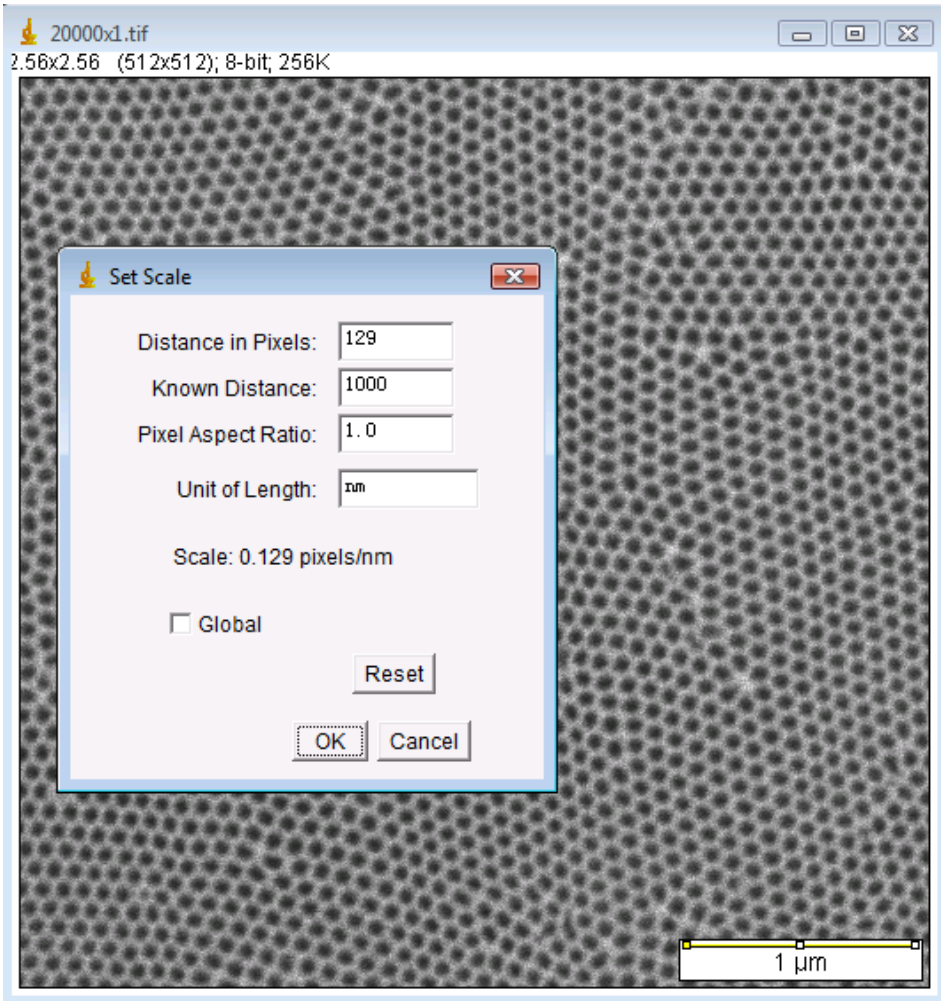

Fig. A2 Set scale in ImageJ

Next step is adjusting the threshold. Choose the image type (8-bit, 16-bit or 32-bit) under main menu **Image** → **Type.** Then adjust the threshold by choosing **Image** → **Adjust** → **Threshold**. Then adjust the threshold to a certain value that makes the red circles cover all the holes (See Fig. A4 and Fig. A3). Press **Set**.

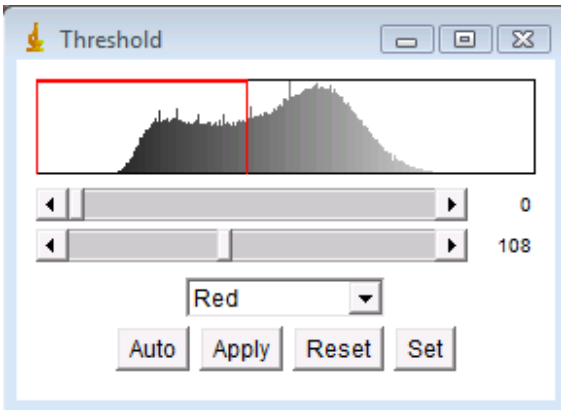

Fig. A4 Adjust threshold in ImageJ.

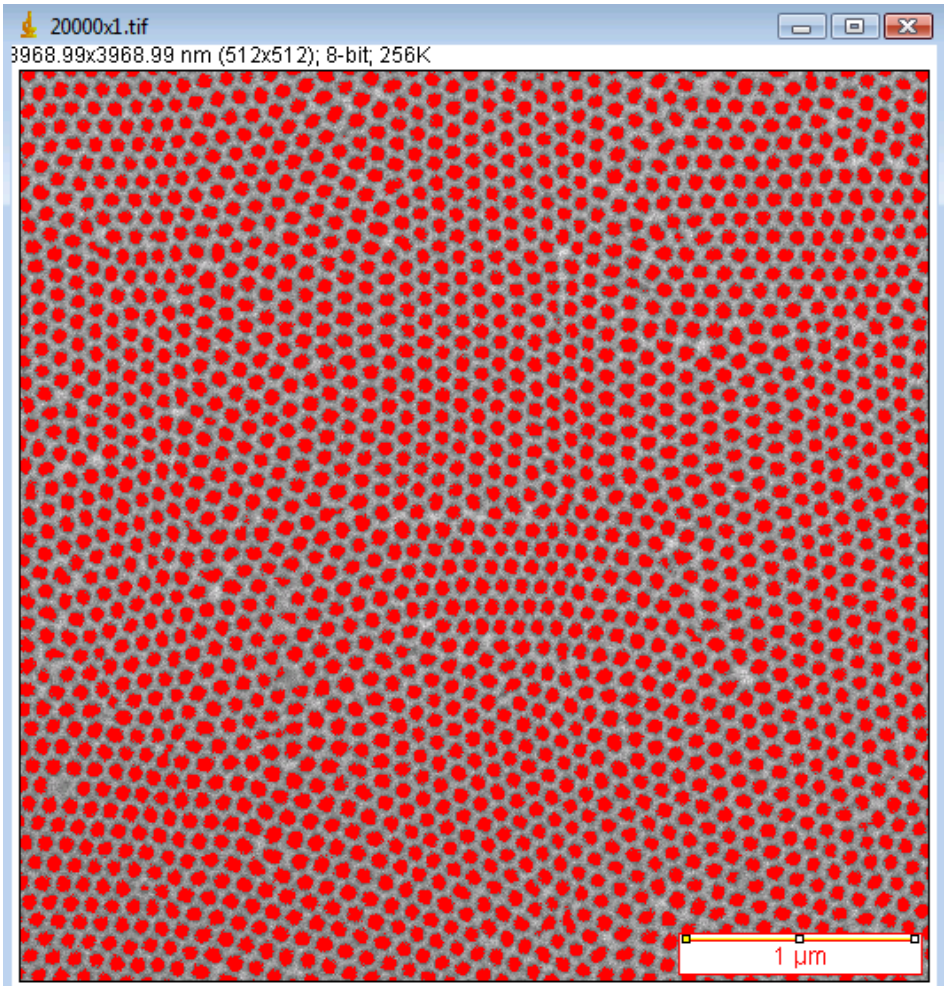

Fig. A3 Threshold adjusting result figure in imageJ.

The following step allows us to get data. Under **Analyze** menu, choose **Set measurement** and select necessary parameters for output. Then choose **Analyze particles**. Refine the size and choose different display under Show catalogue as shown in Fig. A5. Click OK.

Finally, the results figure and a worksheet will pop out (See Fig. A6). Save the sheet as an Excel file. To make final analysis, use the data saved in Excel to calculate desired parameters. From this demonstrated image, 1869 sets of parameters were obtained. As a result, the average diameter of the nanopores is around 76nm with a distribution of 6.2%.

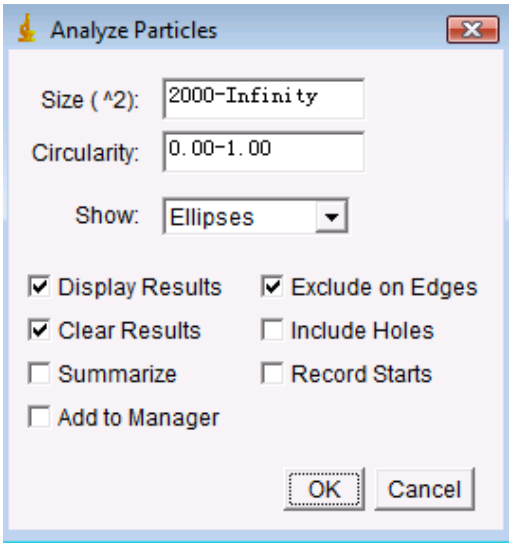

Fig. A5 Analyze particles dialogue window in imageJ.

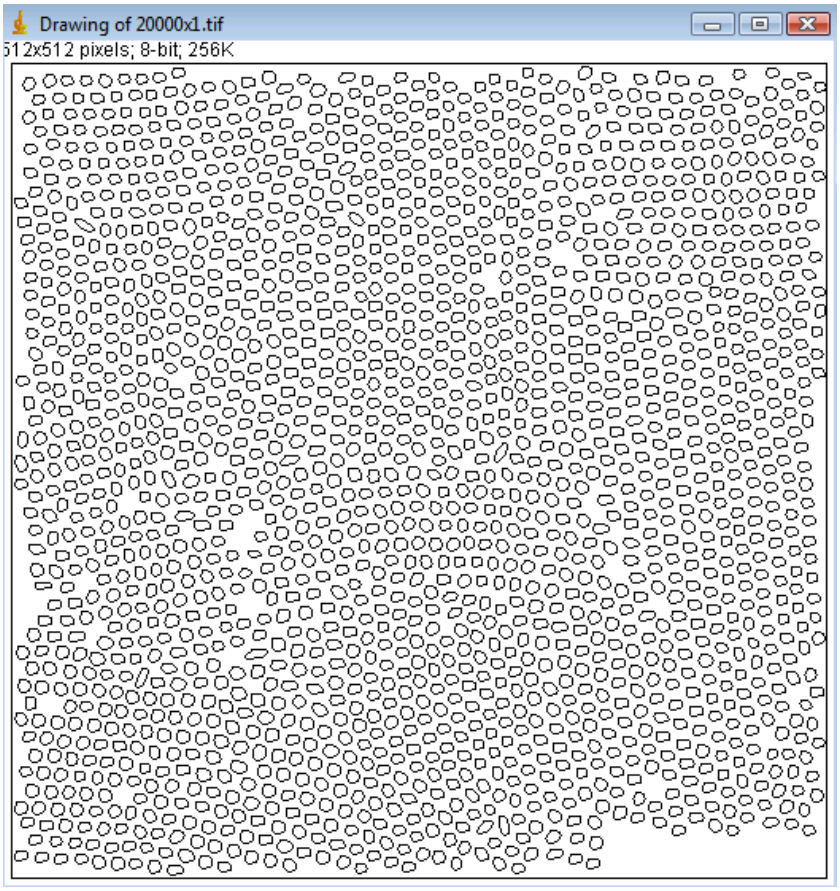

Fig. A6 Analysis result figure in ImageJ.

Appendix B Other image analysis by ImageJ

Using the same analysis procedures demonstrated above, Figure 4.1 (Top-view SEM images of AAO template after two-step anodization), Figure 4.4 (Top-view SEM image of empty homemade AAO template with 50nm thickness gold coating) and Figure 4.11 (b) (top-view SEM images of AAO templates with CNTs inside nanopores after 5h etching) were examined by ImageJ.

Fig. B1 shows the analysis results image of Figure 4.1. The average diameter of the nanopores in AAO templates is around 50 nm and the inter-pore distance (distance from the center of one nanopore to the center of a neighboring nanopore) is about 90nm. The overall packing density is on the order of 10^{10} cm^{-2}.

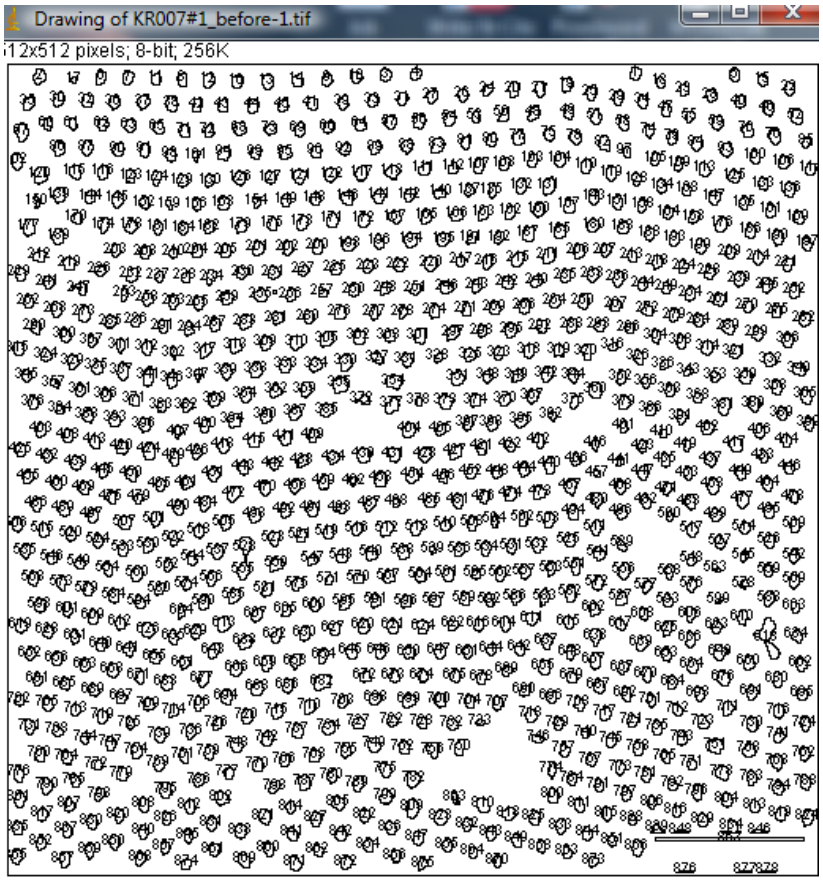

Fig. B1 ImageJ analysis results image of AAO template after pore widening.

Fig. B2 shows the analysis results image of Figure 4.4 . Pores with a diameter of ca. 78nm were observed.

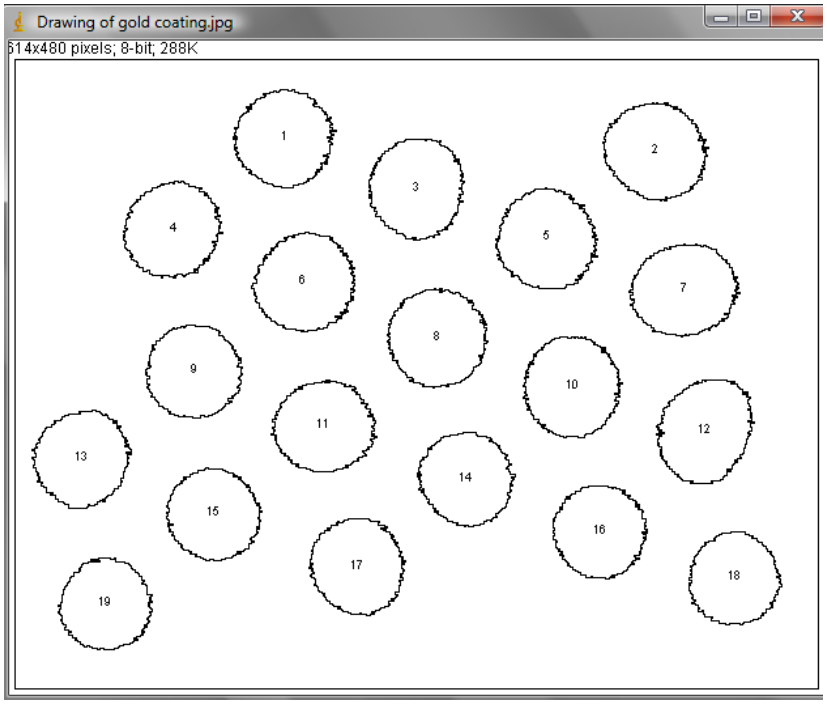

Fig. B2 ImageJ analysis results image of empty homemade AAO template with 50nm thickness gold coating.

Fig. B3 shows the analysis results image of Figure 4.11 (b). The diameter of the opening of nanopore channels decreased to 30 nm.

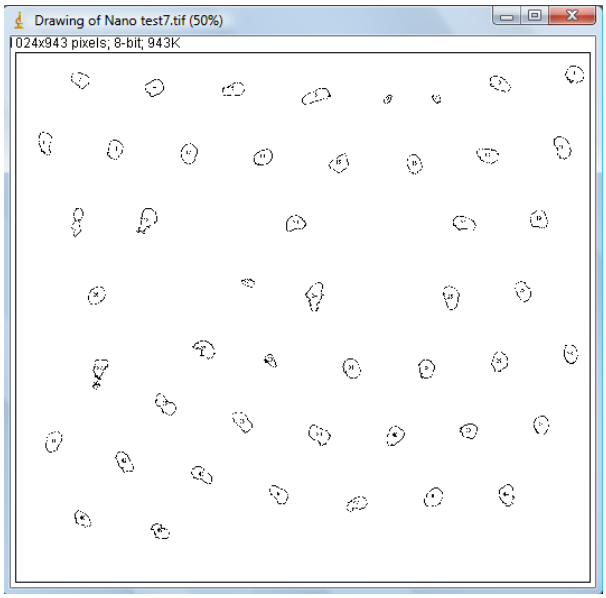

Fig. B3 ImageJ analysis results image of top-view SEM images of AAO templates with CNTs inside nanopores after 5h etching.